*AGU Advances*

Original Version of

# Subantarctic Mode Water Biogeochemical Formation Properties and Interannual Variability

Seth M. Bushinsky and Ivana Cerovečki

[1] Department of Oceanography, School of Ocean and Earth Science and Technology, University of Hawai'i at Mānoa, Honolulu, HI

[2] Scripps Institution of Oceanography, University of California San Diego, La Jolla, CA

# Subantarctic Mode Water Biogeochemical Formation Properties and Interannual Variability

Seth M. Bushinsky[1] and Ivana Cerovečki[2]

[1]Department of Oceanography, School of Ocean and Earth Science and Technology, University of Hawai‘i at Mānoa, Honolulu, HI

[2]Scripps Institution of Oceanography, University of California San Diego, La Jolla, CA

Corresponding author: Seth Bushinsky (seth.bushinsky@hawaii.edu)

**Key Points:**

- **Subantarctic Mode Water formation properties were characterized using biogeochemical Argo float observations over a seven-year period.**
- **Subantarctic Mode Water formed in the Pacific is higher in oxygen, nitrate, and dissolved inorganic carbon than that from the Indian Ocean**
- **Subantarctic Mode Water is undersaturated in oxygen and supersaturated with carbon dioxide at the time of formation.**

**Abstract**

Subantarctic Mode Water (SAMW) is a key water mass for the transport of nutrients, oxygen, and anthropogenic carbon into the ocean interior. However, a lack of biogeochemical observations of SAMW properties during wintertime formation precluded their detailed characterization. Here we characterize for the first time SAMW properties across their entire wintertime formation regions based primarily on biogeochemical profiling floats. Observations show that the SAMW properties differ between the two main formation regions in the Pacific and Indian sectors of the Southern Ocean. SAMW formed in the Pacific is colder, fresher, and higher in oxygen, nitrate, and dissolved inorganic carbon than its Indian Ocean counterpart. The relationship between potential density and biogeochemical water properties is nearly identical between the two formation regions; property differences thus predominantly reflect the difference in mean densities of SAMW formed in each region. SAMW is undersaturated in oxygen during formation, which will impact calculations of derived quantities that assume preformed oxygen saturation. SAMW is at or above atmospheric $pCO_2$ during wintertime and therefore not a direct sink of contemporary carbon dioxide during the formation period. Results from the Biogeochemical Southern Ocean State Estimate suggest anti-correlated interannual variability in the dissolved inorganic carbon, nitrate, and oxygen in the central and southeastern Pacific formation regions similar to previously established patterns in mixed layer variability. This indicates that the mean properties of SAMW will vary depending on which sub-region has a stronger formation rate, which is in turn linked to the Southern Annual Mode and the El-Niño Southern Oscillation.

**Plain Language Summary**

In the Southern Ocean, north of the Antarctic Circumpolar Current, wintertime surface ocean heat loss cools the water, increasing its density and forming thick layers of well mixed water that enter the ocean. This water, called Subantarctic Mode Water (SAMW), represents an important pathway for anthropogenic carbon, nutrients and oxygen into the ocean interior. In this study we used new wintertime observations from profiling robots equipped with sensors that measure oxygen, nitrate, and pH in the top 2000 m to determine important initial properties of SAMW for the first time. We find that the SAMW properties differ between the Pacific and Indian formation regions and are related to the different densities of water formed in each basin. These properties indicate that it is unlikely for SAMW to take up present-day carbon dioxide during formation, though it may

still take up anthropogenic carbon. We investigated how these properties varied year-to-year using an ocean model which assimilates the observations, finding links between changes in the biogeochemical properties and physical processes as well as large-scale climate variability. These results will provide valuable constraints on interpretation of subsurface ocean measurements and model studies investigating the role of these waters in the global carbon cycle.

## 1. Introduction

The Southern Ocean is responsible for 50% of the contemporary carbon absorbed by the ocean each year (DeVries 2014; Le Quéré et al. 2018; Friedlingstein et al. 2019). This contemporary carbon uptake by the Southern Ocean is largely driven by a strong anthropogenic carbon flux overlaid on a balanced natural carbon cycle (Gruber et al. 2019b). North of the Antarctic Circumpolar Current (ACC), the uptake of natural carbon is driven by Thermocline Waters (TW) from the subtropics that cool as they are advected south and are the site of biological production, both of which lower the partial pressure of $CO_2$ ($pCO_2$) in the ocean, drawing down carbon from the atmosphere (Mikaloff Fletcher et al. 2007; Gruber et al. 2009b, 2019b). This uptake is balanced by the upwelling of Circumpolar Deep Water (CDW) enriched in old carbon from degraded biological material that is released to the atmosphere as CDW waters reach the surface south of the ACC. A fraction of the upwelled CDW is advected southward, where it cools and subducts as Antarctic Bottom Water, while another fraction is advected northward, mixing with TWs advected southward, forming mode and intermediate waters (Iudicone et al. 2011; Morrison et al. 2015). Newly formed Subantarctic Mode Water (SAMW) contains a mix of CDW, Antarctic Intermediate Water (AAIW), older SAMW that is re-entrained as intense surface heat loss during the winter drives deep winter mixed layers and subduction, and TW (McCartney 1977; Hanawa and Talley 2001). After subduction, these well-mixed, near-surface layers are advected away from their formation regions into the ocean interior (McCartney 1977, 1982). SAMW primarily forms in the Indian and Pacific sectors of the Southern Ocean, where wintertime mixed layers are deepest (Figure 1).

After subduction, SAMW is advected by the ACC and can either be re-entrained and modified during subsequent winter mixed layer deepening or exported into the ocean interior where it is advected by the subtropical gyre circulation (Hanawa and Talley 2001; Koch-Larrouy et al. 2010; Hartin et al. 2011; Cerovečki et al. 2019; Morrison et al. 2022). SAMW redistributes heat and freshwater from the Southern Ocean to the tropics (Wong et al. 1999) and the export of nutrients from the Southern Ocean through mode and intermediate waters fuels between 44 and 75% of global ocean productivity (Sarmiento et al. 2004; Primeau et al. 2013). SAMW is also one of the major water masses that transports anthropogenic and natural carbon into the ocean interior from the Southern Ocean, based on interior measurements of dissolved inorganic carbon (DIC)

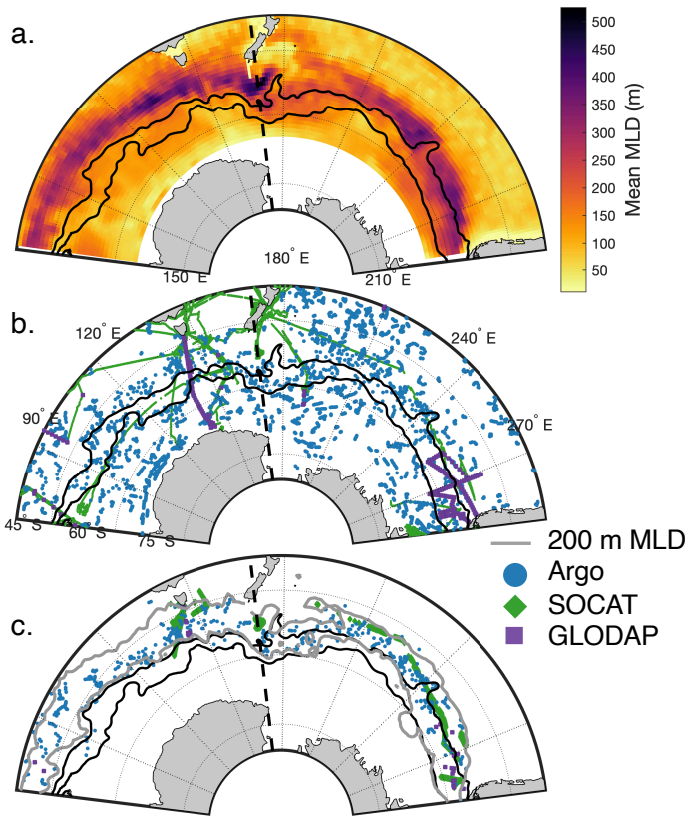


**Figure 1. Wintertime mixed layer depths (MLD) and distribution of wintertime observations in the Indian and Pacific sectors of the Southern Ocean.** (a) Mean winter (Aug. & Sept.) mixed layer depth calculated from gridded Argo product 2005-2020 (RG-Argo). (b) Map of wintertime water column biogeochemical properties (Argo floats, blue dots; GLODAP dataset since 1990, purple squares) and $pCO_2$ surface measurements (SOCAT dataset since 1990, green squares). (c) Same as (b), but only showing data within the SAMW density ranges in the Pacific ($26.8 \leq \sigma_\theta < 27.05$ kg m$^{-3}$) and Indian ($26.6 \leq \sigma_\theta < 26.9$ kg m$^{-3}$) basins within the wintertime mixed layer depths ≥ 200 m. Gray contour represents the mean wintertime 200 m MLD from RG-Argo indicating mode water formation regions. Black lines in all plots are the Polar Front (southern line) and the Subantarctic Front (Orsi et al. 1995).

and modeling inversion studies (Mikaloff Fletcher et al. 2006, 2007; Gruber et al. 2009b, 2019b). Southern Ocean mode and intermediate waters help ventilate the ocean interior with oxygen (Russell and Dickson 2003; Carter et al. 2014) and their distinctive high oxygen signature is evident as they spread into the subtropical gyre (McCartney 1977; Hanawa and Talley 2001). Modeling results indicate that SAMW has accumulated ~20% of the total ocean anthropogenic carbon inventory and gains ~28% of the annual anthropogenic increase, with 60-86% of the increase coming from air-sea fluxes and the rest accumulated through interior diapycnal processes (Groeskamp et al. 2016; Iudicone et al. 2016). However, the mechanistic understanding of air-sea $CO_2$ fluxes that we gain from model representations are dependent on accurate model representation of preformed mode water biogeochemical properties and resulting air-sea fluxes for which validation data has been previously unavailable.

SAMW is not homogeneous in space, but instead consists of pools of water with distinct properties that form in different locations. Water is then exported to the subtropics from these well-defined "hotspots" of formation following distinct pathways influenced by topography (Koch-Larrouy et al. 2010; Herraiz-Borreguero and Rintoul 2011; Li et al. 2021). While many physical

processes play an important role in SAMW formation, air-sea buoyancy fluxes and Ekman transport of cold water are generally considered to be dominant processes (Speer et al. 2000; Sloyan and Rintoul 2001; Rintoul and England 2002). SAMW is strongly coupled to the atmosphere and the interannual variability of wintertime atmospheric forcing governs the interannual variability and regional distribution of SAMW formation in the Pacific and Indian sectors of the Southern Ocean, as revealed by the Argo observations. In the Southern Hemisphere the extratropical atmospheric circulation has the quasi-stationary zonal wave number 3 (ZW3) pattern present in both the mean atmospheric circulation and its variability on daily, seasonal, and interannual timescales (Raphael 2004). As the SAMW is strongly coupled to the atmosphere, the ZW3 can also be imprinted onto the zonal distribution of deep wintertime mixed layers associated with the SAMW formation (Meijers et al. 2019; Tamsitt et al. 2020; Cerovečki and Meijers 2021). The meridional wind anomalies introduced by these MSLP anomalies are of the opposite sign on the two flanks of each center of the MSLP anomaly, resulting in anomalously cold conditions and deep mixed layers on the flank with enhanced southerly winds, and anomalously warm conditions and shallow mixed layers on the flank with enhanced northerly winds. Thus in years with strong wintertime MSLP anomalies in the SAMW formation latitude range, deep wintertime mixed layer depth (MLD) anomalies have a dipole pattern in each of the three ocean sectors, and these MLD anomalies in the three ocean sectors tend to be in phase, which results in a more circumpolar response to the atmospheric forcing (Tamsitt et al. 2020; Cerovečki and Meijers 2021). Argo observations have also revealed that the variability of mode water volume and properties in SAMW pools is governed not only by local atmospheric forcing, but also by advective processes that transport property anomalies eastward, with a ~1 year lag between the central and southeastern Pacific (Meijers et al. 2019; Cerovečki et al. 2019).

SAMW variability is strongly linked to the dominant modes of variability in the Southern Hemisphere. The Southern Annual Mode (SAM) leads to large-scale wintertime MLD anomalies (Sallée et al. 2010), strongly influencing the volume of subducted mode water. This volume has increased over the Argo period (Gao et al. 2018; Portela et al. 2020) as mixed layers have deepened in response to a strengthening SAM (Qu et al. 2020). In the Pacific, the SAMW formation is also influenced by El Niño–Southern Oscillation (ENSO), and the relative phases of the ENSO and SAM governs the interannual variability of SAMW thickness (Meijers et al. 2019).

In contrast to physical properties, changes in large-scale Southern Ocean biogeochemical properties in response to climate variability, including those of SAMW, have primarily been described using the results of model simulations. Modeling studies have linked decreased contemporary Southern Ocean $CO_2$ fluxes and elevated surface DIC concentrations to positive SAM phase through increased Ekman-driven upwelling of old waters enriched in DIC (Lenton and Matear 2007; Lovenduski et al. 2007). Verdy et al. (2007) explored climate drivers of oxygen and $CO_2$ fluxes in the Southern Ocean using a global numerical ocean model. The Pacific dipole described in Meijers et al. (2019) and Cerovečki and Meijers (2021) is evident in the first EOF of both oxygen and $CO_2$ flux variability in Verdy et al. (2007), which the authors also associate with SAM. The upwelling of low oxygen water drives oceanic uptake of oxygen, so the response has the opposite sign from $CO_2$. They find that ENSO is a secondary driver of oxygen and $CO_2$ flux variability in the Pacific with a uniform central Pacific response driven by surface heat fluxes rather than the dipole associated with SAM.

Wintertime measurements of biogeochemical tracers in the Southern Ocean are limited, with most of the shipboard measurements that have historically underpinned our understanding of ocean properties concentrated in a few locations (Figure 1). Therefore, despite its importance in the distribution of carbon, nutrients, and oxygen in the ocean interior, the biogeochemical properties of SAMW at the time of formation are poorly characterized. Knowing water mass formation properties is key to interpreting downstream biogeochemical measurements and ground-truthing the model-based interpretations of the role of SAMW in nutrient export and anthropogenic carbon uptake. The impact of nutrients exported in SAMW to the global ocean on air-sea carbon dioxide fluxes is determined by whether those nutrients are preformed or sourced from biological material that degraded sometime between initial subduction and re-exposure to the surface. Nutrient regeneration from respiration is accompanied by the release of DIC and consumption of oxygen, such that biological production fueled by regenerated nutrients will either be offset by regenerated $CO_2$ outgassing or will re-fix the regenerated DIC back to organic carbon. Preformed nutrients are not coupled to regenerated DIC and can serve to draw carbon down from the atmosphere. Preformed nutrients are often calculated using oxygen measurements, an oxygen consumption to nutrient release respiration ratio, and assumed oxygen saturation during formation. It is therefore important to characterize oxygen and preformed nutrients present in different water masses and to understand if and how they vary in time.

Only one study has analyzed formation properties of SAMW from shipboard measurements made on individual cruises that crossed a SAMW formation region in the Southeast Pacific (Carter et al. 2014). Recent deployments of profiling floats equipped with biogeochemical sensors throughout the Southern Ocean by the Southern Ocean Carbon and Climate Observations and Modeling project (SOCCOM; Johnson et al. 2017) offer a new opportunity to characterize these waters and better understand the role that SAMW plays in the global carbon cycle and production.

While mapped interpolation products are available for some biogeochemical variables (Garcia et al. 2010; Landschützer et al. 2013; Rödenbeck et al. 2013; Lauvset et al. 2016) these products are biased toward summertime measurements. For example, inclusion of float-derived $pCO_2$ with ship-board observations in standard mapping methods has reduced estimates of the annual Southern Ocean contemporary carbon uptake from an annual uptake of ~1.1 Pg C $yr^{-1}$ to 0.75 ± 0.22 Pg C $yr^{-1}$ (Bushinsky et al. 2019), primarily due to new wintertime observations. Furthermore, the wintertime formation of SAMW has strong temporal and spatial variability, leading to possible biases if properties or variability are extrapolated from too-sparse measurements (Fay et al. 2014). These float-derived year-round, vertically-resolved biogeochemical measurements for the first time enable characterization of these important water masses during formation and will provide the link between surface processes and interior ocean properties and changes. In this study we use wintertime observations from profiling floats and available shipboard measurements to characterize SAMW properties at the time of formation. Using results of an ocean state estimate we determine how these properties vary interannually and regionally prior to export into the global ocean.

## 2. Methods

*SAMW identification*

SAMW was identified from gridded Argo T&S (hereafter RG-Argo; Roemmich and Gilson 2009) using a potential vorticity (PV) threshold of PV < 40 x $10^{-12}$ (m $s)^{-1}$, with PV defined as $PV = f/\rho_0 \ \partial\sigma_\theta/\partial z$, where $f$ is the Coriolis parameter, $\rho_0$ is the density of seawater, and $\sigma_\theta$ is the potential density (taken here to be defined relative to the surface), averaged over the years 2005-2020. This PV threshold was used to identify the density range of core SAMW in the Pacific (170°E to 70°W, 64°S to 45°S) and Indian (68°E to 170°E, 55°S to 30°S) ocean sectors, identified

199 as density bins (0.05 kg $m^{-3}$-wide spacing) containing at least 5% of total SAMW volume in an
200 annual average. We then used these density ranges throughout the rest of the study to identify
201 wintertime SAMW in each basin.
202
203 *Biogeochemical observations*
204 Biogeochemical properties of the deep wintertime mixed layers that form mode water were
205 determined from biogeochemical Argo float observations obtained from two sources. The primary
206 dataset is observations from over 200 floats equipped with oxygen, nitrate, pH, and bio-optical
207 sensors deployed by SOCCOM since 2014 (May 2021 snapshot; Johnson et al., 2017). The
208 SOCCOM data are supplemented by the University of Washington Argo Oxygen dataset (v1.1;
209 Drucker and Riser, 2016) that contains post-adjusted Argo oxygen data from 2003 to 2014. Where
210 float data was present in both datasets the SOCCOM data were preferentially used. The final
211 dataset contains 311 floats, of which 53 contain profiles that fell within the criteria used for SAMW
212 formation periods. A profile was determined to have sampled the SAMW formation period if it
213 fell within the density range for a given basin, was from August or September, and had a calculated
214 MLD of at least 200 m.
215 Oxygen and nitrate are measured by sensors mounted on the floats with stated uncertainties
216 of 1-2 μmol $kg^{-1}$ for oxygen and <1 μmol $kg^{-1}$ for nitrate (Johnson et al. 2017). The partial pressure
217 of carbon dioxide ($pCO_2$) and dissolved inorganic carbon (DIC) are estimated in the SOCCOM
218 data processed stream from measured pH and an alkalinity multiple linear regression (Williams et
219 al. 2017; Carter et al. 2018) with a theoretical uncertainty of ~11 μatm for $pCO_2$, and ~6 μmol $kg^{-1}$
220 for DIC (Williams et al. 2017, 2018; Johnson et al. 2017). While float observations underwent
221 prior QC, a secondary QC was performed by checking time series of temperature, salinity, oxygen,
222 nitrate, pH, and derived $pCO_2$ in the upper 20 m for each float. Large spikes in individual properties
223 with no accompanying changes in related properties were removed from analysis (Supplemental
224 Table S1, 116 profiles removed out of 36,247 profiles total).
225
226 *Shipboard observations and derived quantities*
227 Shipboard bottle measurements from the Global Ocean Data Analysis Project v2.2020
228 (GLODAP; Key et al., 2015; Olsen et al., 2016) and underway $pCO_2$ data from the Surface Ocean
229 $CO_2$ Atlas v2021 (SOCAT; Bakker et al., 2016) are used to supplement float observations. $pCO_2$

was calculated from GLODAP DIC and alkalinity using CO2SYS (van Heuven et al. 2011) and the same carbonate system constants as used by the SOCCOM project (Williams et al. 2017). MLDs are calculated for each float and ship profile using a 0.03 kg $m^{-3}$ $\sigma_\theta$ change from a 10 m reference (de Boyer Montégut et al. 2004). SOCAT $pCO_2$ observations are underway measurements that are not associated with a vertical profile from which MLD could be calculated. Instead, SOCAT observations were matched to the closest 1° x 1° ML from objectively interpolated RG-Argo (Roemmich and Gilson 2009) MLDs .

$\Delta pCO_2$ (surface $pCO_2$ minus atmospheric $pCO_2$) values were calculated using the atmospheric $CO_2$ mole fraction ($xCO_2$, NOAA Greenhouse Gas Marine Boundary Layer Reference; Dlugokencky et al. 2019) matched to the nearest latitude. A correction for sea level pressure was applied using a mean annual cycle for each location calculated from a 10-year time series of National Centers for Environmental Prediction (NCEP; Kalnay et al., 1996) reanalysis sea level pressure and water vapor pressure calculated from SST and SSS (Zeebe and Wolf-Gladrow 2001). Oxygen saturation concentrations are calculated from observed temperature and salinity and García and Gordon (1992) solubility coefficients.

*Biogeochemical* Southern *Ocean State Estimate (BSOSE)*

The biogeochemical Southern Ocean State Estimate (BSOSE; Verdy and Mazloff 2017) is a coupled biogeochemical-sea-ice-ocean state estimate that assimilates physical and biogeochemical observations, including from biogeochemical profiling floats, creating a coherent picture of Southern Ocean processes that conserves mass and has closed budgets for biogeochemical properties. BSOSE is forced by optimized atmospheric reanalysis fields from ERA-Interim (Dee et al. 2011). We used iteration 135, covering 2013-2019 at 1/6° resolution, for analysis of interannual variability. Here we only analyze the spatial and temporal variability of SAMW in BSOSE output from the Pacific sector, because the distribution of deep wintertime MLDs and SAMW formation regions in BSOSE iteration 135 was more similar to these from RG-Argo than in the Indian sector.

## 3. Results and discussion

### 3.1 SAMW formation properties

The potential density bounds established for regional SAMWs were $26.8 \leq \sigma_\theta < 27.05$ kg $m^{-3}$ in the Pacific sector and $26.6 \leq \sigma_\theta < 26.9$ kg $m^{-3}$ in the Indian sector. These density ranges agree well with those from the literature (e.g. Cerovečki and Meijers, 2021). We identified SAMW properties from float observations in the Pacific and Indian sectors during the time of formation using these density bounds and calculating mean mixed layer properties from August to September at the locations where the float profile mixed layer depth was at least 200 m. The depth criterion was used to isolate the deep wintertime mixed layers associated with SAMW formation from other shallower winter mixed layers, such as in areas of reventilation or seasonally formed water that does not connect to the ocean interior (Koch-Larrouy et al. 2010). The threshold value was determined by examining the individual float observations.

Pressure vs. time plots of individual floats capture the seasonal cycle of deep mixing in the winter, where the lighter density bound of SAMW outcrops at the surface and newly formed waters bring surface properties into the SAMW layer (Figure 2). As the mixed layer shoals in austral spring, these waters mix in the ocean interior with older SAMW. After leaving Pacific or Indian SAMW formation regions, floats often captured reventilation in other areas, such as float 5904695 that captured moderate wintertime ML deepening in the western Pacific in 2017 (Figure 2). The float was advected eastward by the ACC and captured the process of strong wintertime ML deepening in the Pacific in winters of 2018 and 2019. The subsequent year the float was advected through the Drake Passage and into the Atlantic, where SAMW was reventilated, further modifying the properties of SAMW that were set prior to restratification and isolation from the atmosphere. The current study focuses only on the period of deep winter mixed layers and initial formation properties, leaving reventilation and other post-formation modification processes to later work.

Properties in the deep (> 200 m) winter mixed layers were first averaged in density bins within the geographical bounds of each ocean sector and then weighted by volume to calculate mean and standard deviation (Table 1). SAMW formed in the Pacific Ocean is colder and fresher, with higher oxygen, nitrate, DIC, and $pCO_2$ than SAMW that forms in the Indian Ocean (Table 1, Figures 3a and 3b). The relationship between potential density and each water property is nearly identical between the Pacific and Indian formation regions, indicating that the preformed property

**Figure 2. Trajectory and oxygen measurements from float 5904695.** (a) Float 5904695 was deployed in the western Pacific in May 2016 and followed the Subantarctic Front (northern black line) as it was advected by the ACC into the Atlantic basin in 2020. Southern black line is the Polar Front. (b) Float oxygen measurements from the upper 600 m from 2017 to 2021. SAMW density bounds identified for the Pacific are shown for the lighter (blue, 26.8 kg $m^{-3}$) and denser (black, 27.05 kg $m^{-3}$) boundaries. MLD (gray) increases in the wintertime and the lighter SAMW boundary outcrops. MLs deeper than 200m were identified as waters likely to enter the ocean interior and therefore represent SAMW formation waters. This float captured both initial formation (for example in 2018 and 2019) as well as what appears to be subsequent reventilation in later years as the float passed into the Atlantic Ocean. The shallow deep SAMW boundary in 2016, 2017, and 2020 (black line) and the relatively shallow MLs indicate that these are not core SAMW formation regions, though there is some ventilation and likely modification of SAMW properties. Red dots above (b) correspond to when the float was in the Pacific sector (red lines in panel a.).

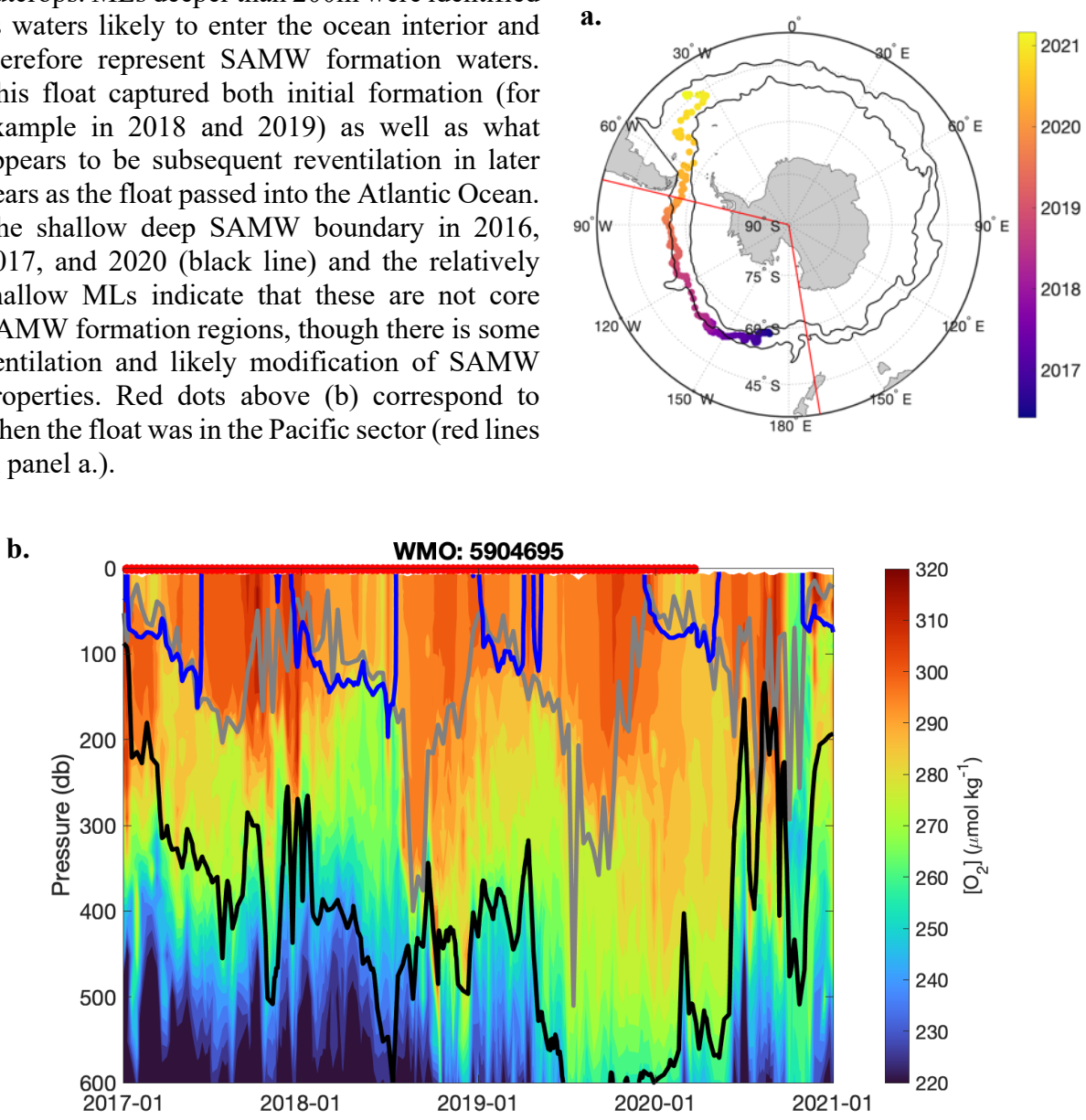


differences are primarily a function of the mean potential density of the waters formed in each region (Figure S1). The relationship between density and ocean properties determined from BGC Argo observations is well represented by BSOSE for all parameters except surface $pCO_2$ (Figure

**Table 1. Mean preformed properties in SAMW formation regions obtained from float observations**

| Region | θ (°C) | Sal. (PSS-78) | $[O_2]$ (µmol kg$^{-1}$) | $[NO_3^-]$ (µmol kg$^{-1}$) | [DIC] (µmol kg$^{-1}$) | $pCO_2$ (µatm) |
|---|---|---|---|---|---|---|
| Pacific | 5.8 ± 0.6 | 34.2 ± 0.1 | 292 ± 6.2 | 21.5 ± 1.2 | 2135.1 ± 7.5 | 419.3 ± 14.4 |
| Indian | 9.3 ± 1 | 34.6 ± 0.2 | 271 ± 8.2 | 13.3 ± 2.9 | 2120 ± 6.3 | 404.4 ± 10.7 |

3, light dashed lines). Southern Ocean $pCO_2$ and the resulting air-sea flux is particularly hard for models to capture due to the non-linear relationship between $pCO_2$ and SST, DIC, and total alkalinity (Mongwe et al. 2018).

One of the few studies to characterize SAMW and the related AAIW properties in this region used data from a cruise in the winter of 2005 (Carter et al. 2014) to characterize deep winter mixed layer properties for SAMW that forms in the southeast Pacific. The SAMW formation properties described in Carter et al. (2014) fall on the denser end of newly formed SAMW in the Pacific, as expected, since the southeast Pacific is where the coldest and freshest SAMW is found. Thus, the Carter et al. (2014) estimates are 0.9-1.4 °C colder and 0.05-0.01 PSU fresher than the mean Pacific SAMW properties described in this study. The Carter et al. (2014) samples fall within ± 1 sd of the property-density relationships described in Figure 3a and 3b for θ, salinity, and $[O_2]$ (gray symbols in Figure 3). The Carter et al. (2014) $[NO_3^-]$ is ~2.9 µmol kg$^{-1}$ lower than the $[NO_3^-]$ observed in this study, indicating that either the SAMW formation region sampled in this study has a greater fraction of older water with a stronger signal of respiration or that less biological production has occurred since that water has been at the surface, either of which could result in a higher $[NO_3^-]$ value. The [DIC] and the $pCO_2$ calculated from the Carter et al. (2014) [DIC] and alkalinity are correspondingly lower than observed values. Correcting for the different amount of biological activity using an assumed Redfield stoichiometry of 106C: 16N and recalculating the [DIC] and $pCO_2$ (in the latter case, also correcting for SST and the biological impacts on alkalinity) yields values that are within the uncertainty of our observed property relationships with density (Figure 3, black symbols). This indicates that there is no fundamental disagreement between the carbonate system values derived from these float measurements and those observed by Carter et al. (2014). The $[NO_3^-]$ and [DIC] differences between the Carter et al. (2014) results and the current study may indicate variability or change on a multi-year time scale and warrants further exploration with longer time-series of observations or model output. The wide range of biogeochemical

properties across the density range of newly formed SAMW illustrates the need for observations that span the entire density and spatial extent of newly formed SAMW to fully characterize properties at the time of formation.

A recent study used ocean observations and a transport model to estimate preformed properties of oxygen, nitrate, silica, phosphate, and total alkalinity throughout the ocean interior (Carter et al. 2021). To compare Carter et al. (2021) to the current values for SAMW we applied the same geographic bounds for the Pacific and Indian regions and masked results using the RG-Argo mean winter MLD criteria of >200m. This yielded preformed properties at 200m depth of 284.8 ± 13.3 μmol kg$^{-1}$ [$O_2$] and 22.3 ± 3.9 μmol kg$^{-1}$ [$NO_3^-$] in the Pacific and 257.6 ± 8.0 μmol

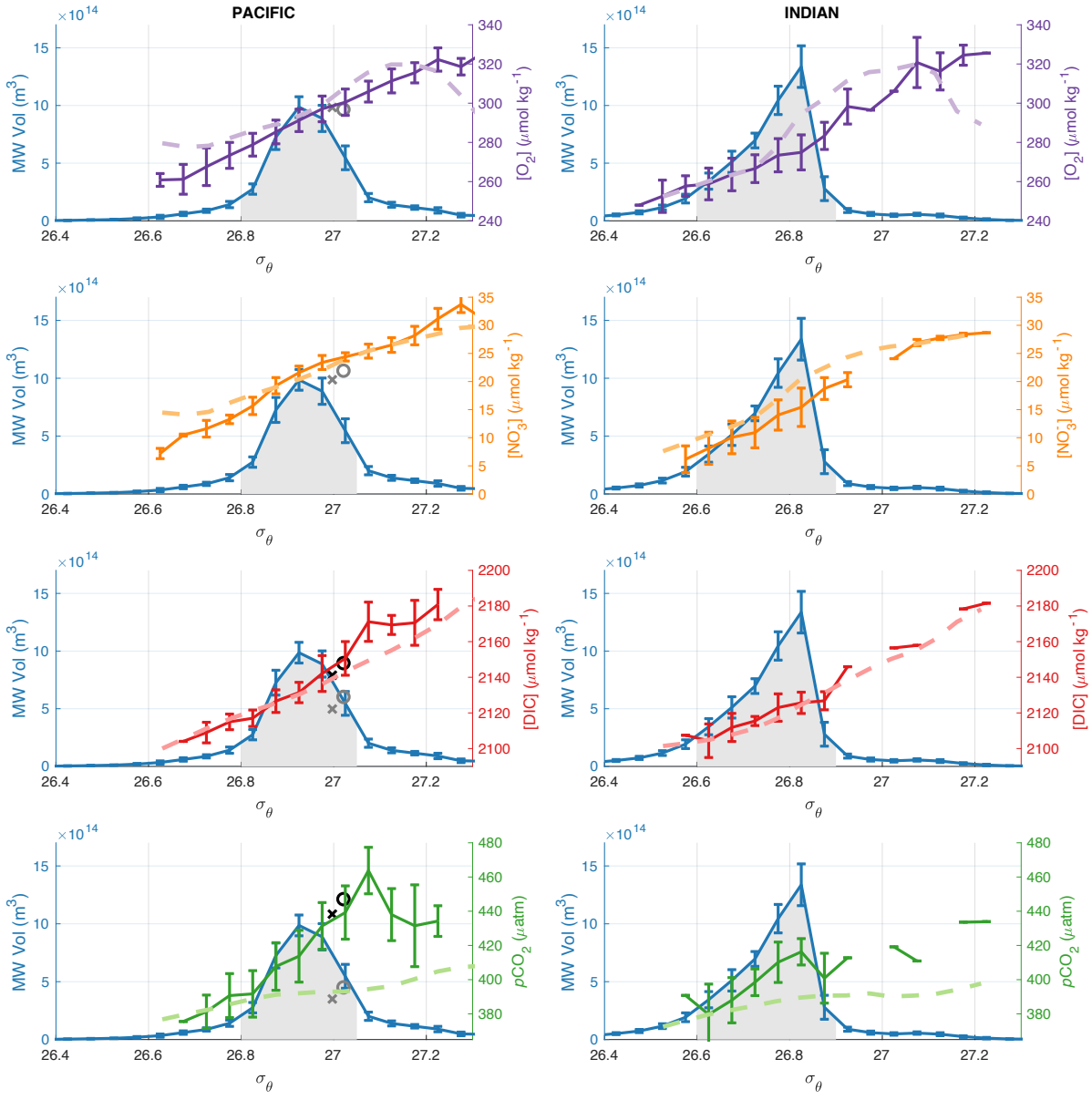

**Figure 3a (previous page). Mixed layer biogeochemical properties of SAMW during wintertime formation and SAMW volume.** Mode water volume and oxygen and nitrate, and estimated DIC and $pCO_2$ are plotted as a function of potential density. The blue curves show the monthly mean volume of water within the ML that satisfies the low potential vorticity (PV) criteria PV<$40\times10^{-12}$ $s^{-1}$ $m^{-1}$, obtained from the RG-Argo data set, for months August and September, 2005-2020, and binned into 0.05 kg $m^{-3}$ wide density bins with the standard deviations indicating the interannual variability. The shaded areas under the volume curves indicates the density bins that contain at least 5% of SAMW by volume. Colored lines with error bars indicate the average properties ± 1 s.d. from biogeochemical floats, binned into the same 0.05 kg $m^{-3}$ wide density bins. Volume and property data are from mixed layers that exceed 200 m. Dashed lines are the August-Sept. mean biogeochemical properties from five-day averaged output from the Biogeochemical Southern Ocean State Estimate (BSOSE) and time averaged over years 2013-2019 where five-day averaged MLDs are deeper than 200m. Overlaid on the Pacific plots are markers indicating the SAMW formation properties identified in Carter et al. (2014) from their "North-Deep Mixed Layer Water" (northwest SAMW outcrop region, gray x's) and "South-Deep Mixed Layer Water" (southeast SAMW outcrop region, gray o's) samples. The Carter et al. (2014) [$NO_3^-$] is an average of 2.9 µmol $kg^{-1}$ lower than this study's observations in the same density range. Adjusting the Carter et al. (2014) DIC and $pCO_2$ for the equivalent difference in organic matter (plus change in alkalinity due to organic matter respiration and SST difference for $pCO_2$) yields DIC and $pCO_2$ shown by the black x's and o's. The longitude range of the Indian Ocean sector is 68-170°E, and the Pacific sector 170-290°E.

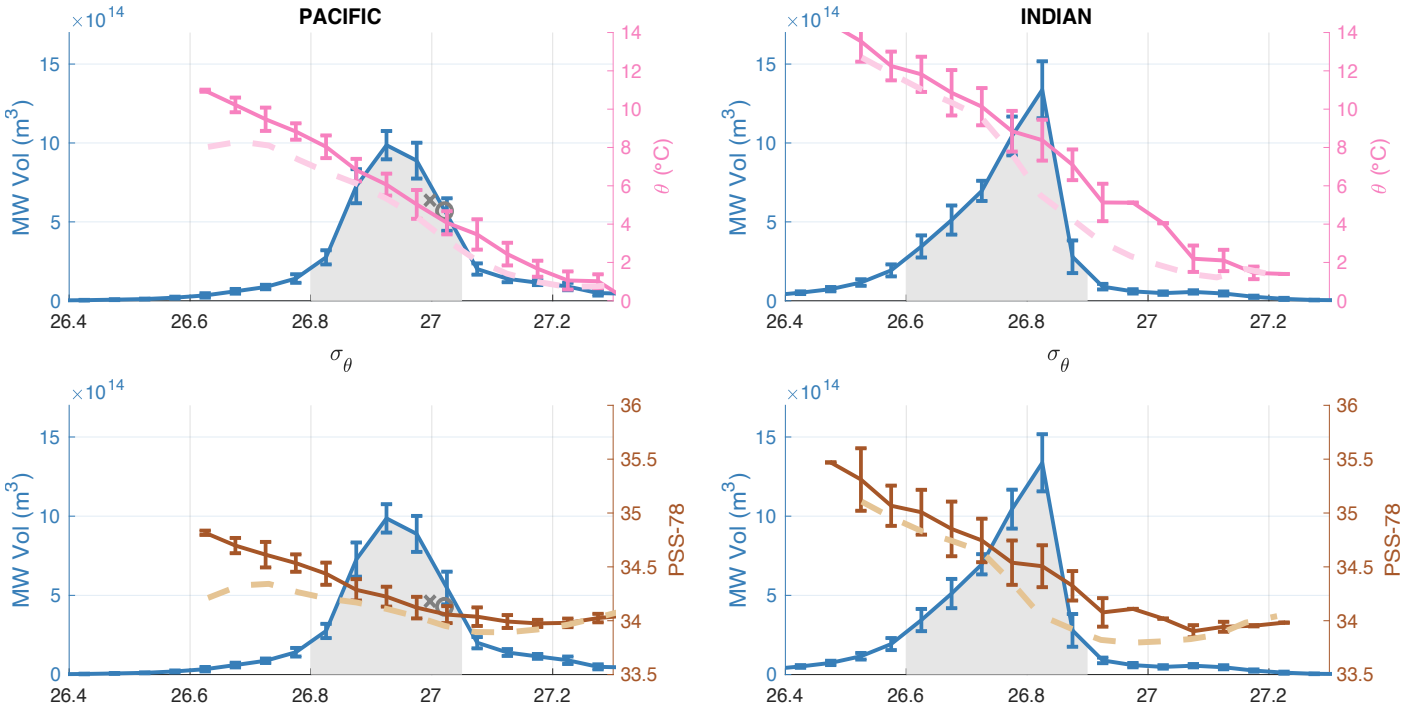


**Figure 3b. Equivalent to Fig 3a but for potential temperature and salinity.**

329

330 $kg^{-1}$ [$O_2$] and 13.4 ± 3.6 μmol $kg^{-1}$ [$NO_3^-$] in the Indian Ocean. The differences in [$O_2$] between
331 Carter et al. (2021) and the current study are on the same order as the difference between currently
332 observed oxygen and the saturation value, potentially introducing biases that would impact
333 interpretation of interior ocean processes. Comparison between the results of Carter et al. (2021)
334 and the current study is limited by the lack of density information from the Carter et al. (2021)
335 results, so it is unclear whether the possible bias between these results is meaningful or an artifact
336 of interpretation.

337 The relative properties of Pacific and Indian formation regions can be broadly interpreted
338 using the property and density relationship described in Figure 3 as differences in mixing fraction
339 of TW and AAIW/CDW in SAMW formation. The Indian SAMW formation region, which is
340 located further north than the formation region in the Pacific, displays a greater influence of TW
341 coming from the subtropics with higher temperatures and lower nutrients and carbon, whereas the
342 Pacific SAMW formation region has a greater influence of upwelled deep water, with high carbon
343 and nutrients, and cold temperatures. Oxygen concentrations follow the north-south temperature
344 gradient, as oxygen air-sea exchange is fast relative to that of $CO_2$, allowing the mixed layer to
345 come close to solubility equilibrium with the atmosphere rather than being controlled by the initial
346 [$O_2$] of the mixing water masses. The interpretation that preformed biogeochemical properties are
347 dependent on the mixing fraction is consistent with our physical understanding of how mode
348 waters form in these two regions. An early analysis of the Southern Ocean State Estimate found
349 SAMW forming in the Indian Ocean to have a greater fraction of volume transformed from the
350 lighter (TW) waters than the Pacific (Cerovečki and Mazloff 2016). The difference between the
351 mean SAMW biogeochemical properties in the Indian and Pacific regions shown in Figure 3a
352 indicates that, at a minimum, properties of newly formed SAMW will change depending on the
353 relative volumes of water formed in each SAMW formation region or within different density
354 classes in a region. This may be critical for projection of future Southern Ocean conditions as the
355 predicted poleward intensification of Southern Ocean winds may impact mode water subduction
356 rates differently in the Indian and Pacific formation regions (Downes et al. 2017). While we now
357 have sufficient data to describe the mean SAMW formation properties in the Pacific and Indian
358 Oceans, these basin-wide averages likely mask the intra-basin differences documented for the
359 physical properties, but observational coverage alone is of insufficient density to convincingly
360 explore intra-basin biogeochemical differences.

### 3.2 Oxygen and carbon dioxide saturation at the time of formation

SAMW is undersaturated in oxygen at the time of formation in both the Pacific and Indian formation regions (Table 2, Figure 4). Wintertime SAMW $\Delta[O_2]$, or the observed oxygen concentration minus saturation concentration ($\Delta[O_2] = [O_2]_{\text{measured}} - [O_2]_{\text{satuturation}}$, $\mu\text{mol kg}^{-1}$), is negative in almost all individual float observations and in all monthly averages, consistent with the sparse observations available in these wintertime locations in the GLODAP v2.2020 shipboard dataset. Mean Pacific SAMW formation waters have a $\Delta[O_2]$ of -11.1 ± 2.3 μmol kg$^{-1}$ and -7.7 ± 2.7 μmol kg$^{-1}$ for Indian SAMW (Table 2, average of float and GLODAP data). During the formation period, high winds drive strong gas exchange and an oxygen flux into the ocean driven by the undersaturated waters. $\Delta[O_2]$ is calculated with an assumption of a standard sea level pressure (SLP) of 1013.25 mbar (1 atm). SLP in the Southern Ocean is typically below 1013.25 mbar and accounting for the mean winter SLP in the Pacific and Indian formation regions would reduce ~30% of the oxygen undersaturation. The fact that the waters stay undersaturated throughout the wintertime formation period indicates that a combination of surface cooling by atmospheric heat loss and continued entrainment of low oxygen sub-surface waters is maintaining undersaturation through the time of water mass formation and subduction.

**Table 2. Mean $\Delta[O_2]$ and $\Delta pCO_2$ of SAMW at the time of formation**

| | [1]$\Delta[O_2]$ (μmol kg$^{-1}$) | | | [2]$\Delta pCO_2$ (μatm) | | | |
|---|---|---|---|---|---|---|---|
| **Region** | **Argo** | **GLODAP** | **Combined Argo & GLODAP** | **Argo** | **GLODAP** | **SOCAT** | **Combined Argo & SOCAT** |
| **Pacific** | -11.1 ± 2.3 | -12.2 ± 1.7 | -11.1 ± 2.3 | 23.9 ± 14.7 | 20.1 ± 0.5 | 5.7 ± 3.6 | 16.1 ± 14.5 |
| **Indian** | -7.9 ± 2.4 | -6 ± 4.3 | -7.7 ± 2.7 | 9.3 ± 11.7 | -14 ± 16.4 | -6.4 ± 7.5 | 0.1 ± 12.2 |

[1] $\Delta[O_2] = [O_2]_{ML,observed} - [O_2]_{saturation}$ ; $O_2$ saturation calculated as a function of temp. and sal. (Garcia and Gordon, 1992)

[2] $\Delta pCO_2 = pCO_{2,surf} - X_{CO_2} \times (\frac{SLP}{1013.25} - pH_2O)$; $X_{CO2}$ from the NOAA Greenhouse Gas Marine Boundary Layer Reference (Dlugokencky et al. 2019), sea level pressure (SLP) in mbar, $pH_2O$ calculated as a function of temperature and salinity (Zeebe and Wolf-Gladrow, 2001).

Undersaturation of oxygen at the time of water mass formation has long been discussed as a difficulty in interpreting interior ocean oxygen measurements, but estimates of preformed oxygen undersaturation have primarily come from model results. Model results have indicated significant oxygen undersaturation during deep water formation in the North Atlantic and Southern Ocean (Ito et al. 2004; Duteil et al. 2013). The assumption that water masses are in equilibrium with

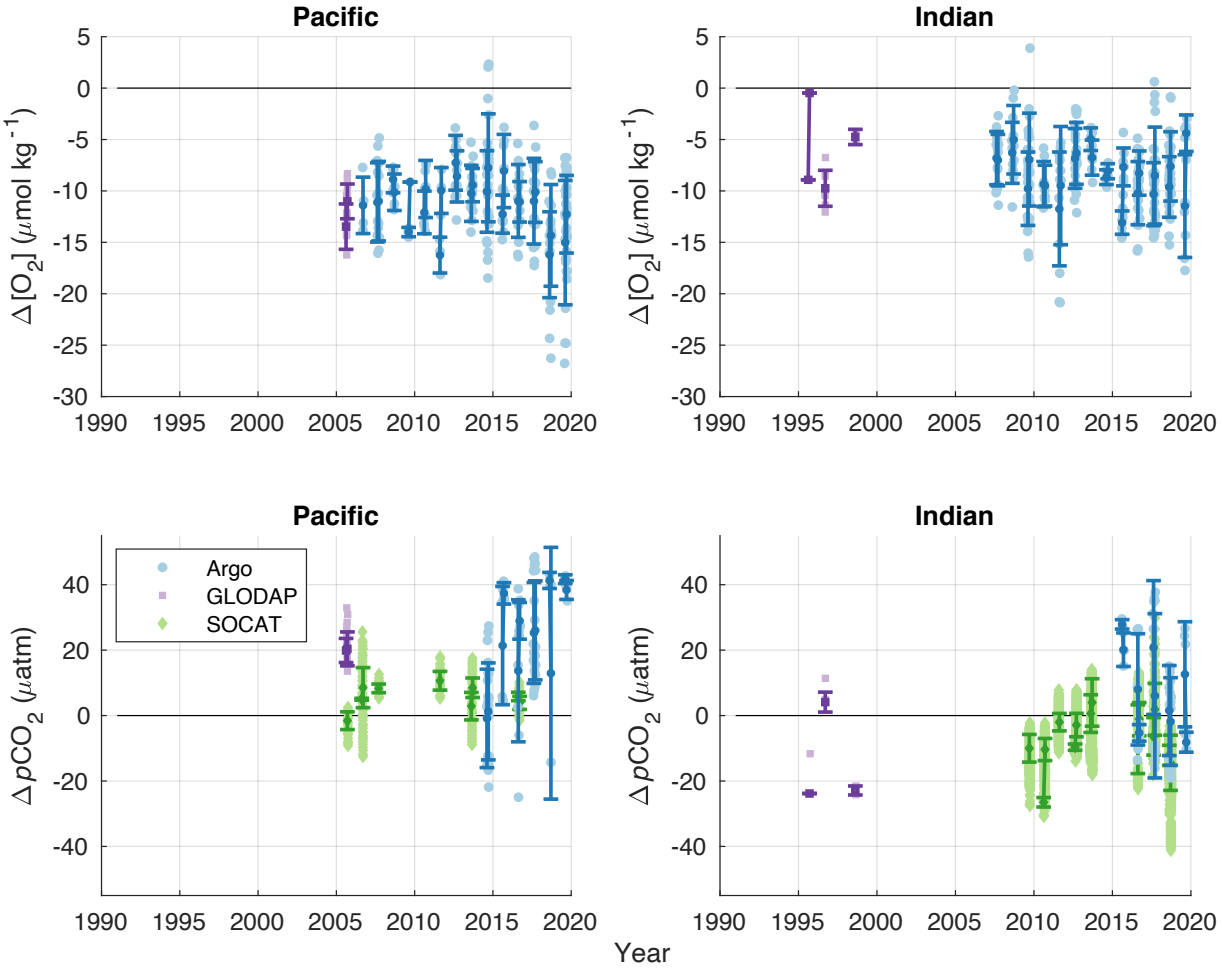


**Figure 4. $\Delta pCO_2$ and $\Delta[O_2]$ in SAMW formation regions from Argo floats and shipboard observations.** (Top row) $\Delta[O_2]$ is calculated using the mixed layer average oxygen concentration from Argo floats (blue circles) and GLODAP shipboard measurements (purple squares) and is not corrected for local atmospheric pressure, reflecting the use of interior oxygen measurements relative to saturation concentration with an assumed atmospheric pressure of 1 atm. (Bottom row) $\Delta pCO_2$ values from SOCAT $pCO_2$ measurements (green diamonds), Argo ph-derived $pCO_2$ estimates, and GLODAP DIC and alkalinity measurements using CO2SYS (van Heuven et al., 2011). SOCAT data are from near-surface underway systems, Argo data from the shallowest observation (typically 5-7m depth), and GLODAP data are from the upper 25m due to data availability. $\Delta pCO_2$ for all data sources were calculated from NOAA ESRL atmospheric $CO_2$ values, corrected for water vapor pressure, and a 2011-2020 climatological sea

383 atmospheric oxygen underpins one of the most common uses of interior ocean oxygen
384 measurements, calculation of apparent oxygen utilization (AOU; $\mathrm{AOU} = [\mathrm{O_2}]_{\mathrm{saturation}} -$
385 $[\mathrm{O_2}]_{\mathrm{measured}}, \mu\mathrm{mol\,kg^{-1}})$, where $[\mathrm{O_2}]_{\mathrm{saturation}}$ is determined from temperature and salinity
386 dependent oxygen solubility (García and Gordon 1992). This quantity is key to determining
387 preformed quantities through the stoichiometric relationship between the consumption of oxygen
388 and release of nutrients and DIC during respiration (e.g.. Mackay and Watson 2021). Oxygen
389 utilization rates (OUR) describe the average respiration in a parcel of water by combining apparent
390 oxygen utilization (AOU) and an age tracer and, again, typically rely on the assumption that
391 preformed oxygen is at saturation. While one study (Koeve and Kähler 2016) found that
392 undersaturation in preformed oxygen did not make large difference in calculated OUR due to other
393 offsetting errors, this was based on a single model and did not have the observations to evaluate if
394 that model properly represented preformed biogeochemical properties.

395 The increasing number of oxygen-equipped profiling floats deployed throughout the ocean
396 is enabling the first observational studies of wintertime oxygen saturation over large areas. The
397 first basin-scale description of mixed layer $\Delta[\mathrm{O_2}]$ and air-sea oxygen fluxes over several years was
398 also conducted in the Southern Ocean using Argo-oxygen floats, finding broad regions of
399 undersaturated wintertime waters but without focusing on specific water masses or ventilation
400 regions (Bushinsky et al. 2017). In the Labrador Sea, Wolf et al. (2018) used Argo-oxygen floats
401 to quantify significant undersaturation in Labrador Sea water at the time of formation that would
402 bias AOU and derived biogeochemical properties. In the study that estimated preformed properties
403 globally (Carter et al. 2021), errors in calculations of AOU were greatest in water formed in the
404 Southern Ocean and in the North Pacific due to the strong degree of wintertime oxygen
405 undersaturation in these regions. Broecker and Peng (1982) introduced the concept of True Oxygen
406 Utilization (TOU), which is the difference between preformed oxygen concentration and the
407 observed concentration, to account for the expected undersaturation during water formation events.
408 Here we show for the first time in SAMW using direct observations of the wintertime formation
409 that SAMW is undersaturated in oxygen when it leaves the ocean surface, altering the
410 interpretation of observations in this water mass throughout the ocean interior and allowing for the
411 calculation of TOU.

412 Mean monthly derived $\Delta pCO_2$ determined only from float observations (surface $pCO_2$
413 minus atmospheric $pCO_2$) is positive in the Pacific (22.5 ± 13.5 µatm) formation region and

slightly positive in the Indian SAMW formation region (9.5 ± 12.9 µatm) (Table 2; Figure 4, bottom). In both the Pacific and Indian SAMW formation regions the $\Delta pCO_2$ calculated from float observations overlaps with, but is generally higher than, either direct shipboard measurements (SOCAT) or derived $\Delta pCO_2$ from paired DIC and alkalinity measurements (GLODAP). SOCAT $pCO_2$ observations are direct measurements with accuracy better than 5 µatm (including quality flags A-D, Lauvset et al. 2017)**,** while the float-derived $pCO_2$ estimates utilize a recently developed technique with a theoretical uncertainty of approximately ± 11 µatm (Williams et al. 2017). Float observations have previously shown higher $pCO_2$ during the winter than has been recorded in the SOCAT database (Gray et al. 2018; Williams et al. 2018). This elevated wintertime $pCO_2$ yields a reduction in the Southern Ocean (south of 35°S) $CO_2$ sink in 2015-2017 from 1.1 Pg C $yr^{-1}$ based on SOCAT data alone to 0.75 Pg C $yr^{-1}$ using a combined SOCAT and SOCCOM dataset (Bushinsky et al. 2019). These results have been challenged, most recently by a study using atmospheric $CO_2$ measurements and atmospheric transport models to constrain the Southern Ocean sink (Long et al. 2021), which yielded a stronger Southern Ocean $CO_2$ sink, though with overlapping uncertainties between the atmospheric constraint and the SOCCOM and SOCAT float-based results in all months where atmospheric data existed.

The key question for average values of $\Delta pCO_2$ or air-sea fluxes is whether averaged float estimates of $pCO_2$ are accurate, not whether individual observations are precise. Crossover comparisons between ship and float $pCO_2$ have indicated a possible high bias of float $pCO_2$ by ~4 µatm (Fay et al. 2018; Gray et al. 2018; Williams et al. 2018), smaller than the differences between the Argo and SOCAT mean values in Table 2. An updated crossover comparison with the addition of a filter eliminating crossover density differences >0.03 kg $m^{-3}$ yields a mean float-derived $pCO_2$ bias of -1.86 ± 15.8 µatm (SOCAT minus floats, n = 52, Supplemental Figure S2), which makes it unlikely that an error in the $pCO_2$ estimation method is responsible for the 17-20 µatm difference in $\Delta pCO_2$ between the mean Argo and SOCAT values observed here.

The difference between the SAMW formation $\Delta pCO_2$ from SOCAT and Argo is more likely due to the differences in sample distribution within each of these formation regions. The strong coupling of density and biogeochemical properties seen in Figure 3 highlights the importance of sampling the full range of densities. Previous work demonstrating spatial variability in physical formation properties of SAMW indicates that spatial variations in biogeochemical properties are also likely to exist. Histograms of the relative frequency of $\Delta pCO_2$, longitude, $\sigma_\theta$,

and θ of mode water formation region observations by the Argo and SOCAT datasets identify differences in the sample distributions of these observations (Figure 5). In the Pacific, SOCAT-determined $\Delta pCO_2$ has a peak of ~0 μatm and a tail toward positive values. The SOCAT observations are primarily from ~170°E, at the very western edge of the Pacific basin, while one cruise crossed the Pacific in 2006. This results in observations that are primarily from $\sigma_\theta$ 26.88 – 26.9 kg $m^{-3}$ and θ of 7.26 – 7.94 °C. Float observations cover a broader range of locations within the Pacific and are consequently spread more evenly across the SAMW density range. SOCAT sample coverage in the Indian Ocean is primarily from cruises originating from Tasmania and do not cover the large formation regions in the central and western Indian Ocean. There are relatively few GLODAP-derived $\Delta pCO_2$ values in either basin, so our best estimate of the $\Delta pCO_2$ for each region is an average of monthly values from the SOCAT and Argo datasets, yielding 16.1 ± 14.5 μatm $\Delta pCO_2$ in the Pacific and 0.1 ± 12.2 μatm $\Delta pCO_2$ in the Indian Ocean.

The entire Southern Ocean is a significant sink for contemporary carbon, mainly driven by the increase in atmospheric anthropogenic carbon and resulting oceanic anthropogenic uptake (Mikaloff Fletcher et al. 2006; Gruber et al. 2009b; DeVries 2014). Much of this anthropogenic carbon is both stored in and exported by mode and intermediate waters (Sabine et al. 2004; Mikaloff Fletcher et al. 2006; Álvarez et al. 2009; Gruber et al. 2009a; Sabine and Tanhua 2010). Model-derived calculations of anthropogenic carbon uptake use the difference in ocean carbon fluxes and accumulation between model runs that do and do not include increasing atmospheric carbon to determine uptake rates of anthropogenic carbon (Iudicone et al. 2011, 2016; Groeskamp et al. 2016). This approach relies on an accurate representation of water mass properties and the physical and biogeochemical processes that influence the carbonate system in models, which have been shown to have difficulty in capturing the seasonal cycle of $pCO_2$ and air-sea $CO_2$ fluxes in the Southern Ocean (Mongwe et al. 2018). If the models do not accurately capture contemporary carbon uptake, then the anthropogenic carbon fluxes and storage will be biased.

Recent work attempting to constrain the magnitude of wintertime outgassing in the Southern Ocean (Gray et al. 2018; Bushinsky et al. 2019; Mackay and Watson 2021; Sutton et al.

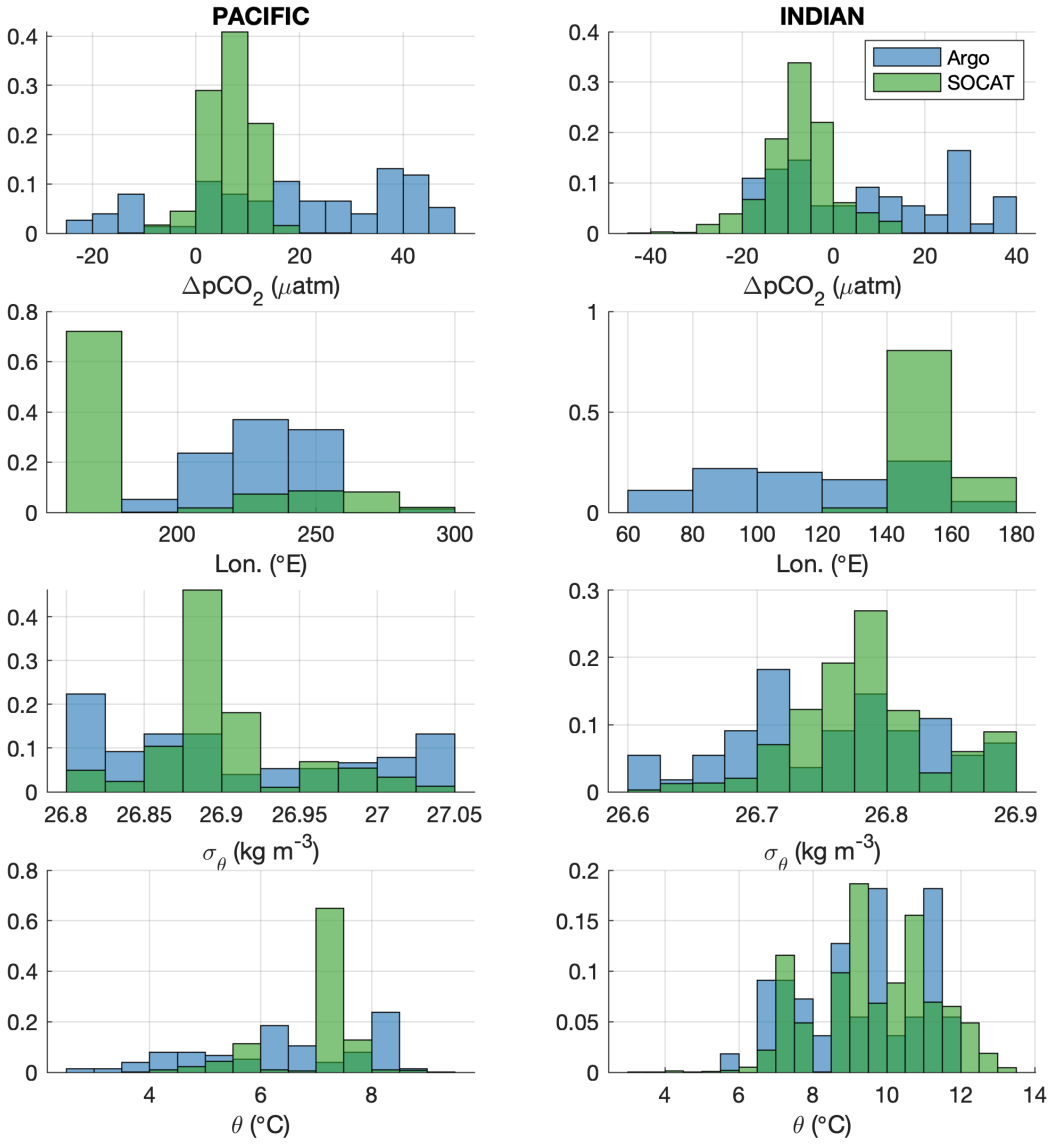


**Figure 5. Properties associated with $\Delta pCO_2$ calculated from SOCAT and Argo.** Relative frequency histograms of calculated $\Delta pCO_2$ and the associated longitude, potential density, and potential temperature for SAMW formation properties in the Pacific and Indian Oceans. SOCAT $\Delta pCO_2$ values are primarily from narrow geographic regions in the Pacific sector near New Zealand and in the Indian sector near Tasmania. BGC Argo data are spread across the sectors, with more distributed density and potential temperature values as well. $\Delta pCO_2$ for SOCAT is similarly within relatively narrow ranges for both sectors, while Argo-derived $\Delta pCO_2$ overlaps with and, on average, is higher than SOCAT $\Delta pCO_2$. GLODAP-derived $\Delta pCO_2$ and associated properties are not shown, as they represent a much smaller sample range and were not included in the property averages (Table 2).

2021; Long et al. 2021) makes it all the more important to understand the mechanisms that could contribute to total Southern Ocean uptake of contemporary and anthropogenic carbon. A $\Delta pCO_2$ during formation that is near or above zero indicates that SAMW does not contribute to the total Southern Ocean contemporary carbon uptake during formation. It is clear from observed accumulation of anthropogenic carbon interior in the ocean interior (Sabine et al. 2004; Mikaloff Fletcher et al. 2006; Sabine and Tanhua 2010; Gruber et al. 2019a) that SAMW is important for the storage of anthropogenic carbon and export to the ocean interior, but the modeling work that has sought to elucidate whether SAMW accumulates anthropogenic carbon through surface or interior processes has not had robust observations for validation (Iudicone et al. 2011; Groeskamp et al. 2016). Here we provide both the mean biogeochemical properties and their distribution with respect to water mass density that can be used to validate model property distributions and representation of contemporary carbon fluxes, thereby improving future estimates of the magnitude and mechanisms of anthropogenic carbon uptake.

### 3.3 Spatial and interannual variability of SAMW formation properties

Almost 15 years of Argo observations have provided invaluable information about strong interannual and spatial variability of SAMW physical properties. Argo observations have revealed that the strong wintertime MLD anomalies in the Pacific, Indian, and Atlantic sectors that develop in some years and are associated with SAM and ENSO tend to be out of phase in the western and eastern parts of ocean sectors (Meijers et al. 2019; Tamsitt et al. 2020; Cerovečki and Meijers 2021). In years with anomalously strong formation of colder and denser varieties of SAMW in the eastern parts of the Indian and Pacific sectors, the formation of warmer and lighter varieties of SAMW in the western part of both ocean sectors is anomalously weak, enhancing the net cooling and densification in each ocean sector. Conditions reverse in years with the preferential formation of warmer and lighter varieties of SAMW (Cerovečki and Meijers 2021). Anomalies that develop in the western part of one ocean sector can subsequently be advected by the ACC to arrive approximately one year later to the eastern SAMW formation region of the same ocean sector (Meijers et al. 2019; Cerovečki et al. 2019). This pattern of an east-west dipole in MLD anomalies and propagation of strong anomalies is evident in the BSOSE Aug-Sept. time-mean MLD (Figure 6). During the 2013-2019 period of BSOSE model simulation analyzed here, the strongest MLD anomalies developed in 2016 when a strong El Niño event coincided with a strong positive SAM

early in the year (Figure 6a). By austral winter 2016, both indexes transitioned to strongly negative (Meijers et al. 2019). The in-phase atmospheric modes resulted in anomalously deep and cold wintertime mixed layers in the central Pacific, and anomalously shallow and warm mixed layers in the southeast Pacific (Meijers et al. 2019; Cerovečki et al. 2019).

In addition to the previously described temperature anomalies (not shown) associated with the 2016 MLD anomalies, BSOSE displays high DIC and high $NO_3^-$ in the central Pacific and low DIC and $NO_3^-$ in the eastern Pacific (Figure 6b). The opposite pattern is observed in 2015, when

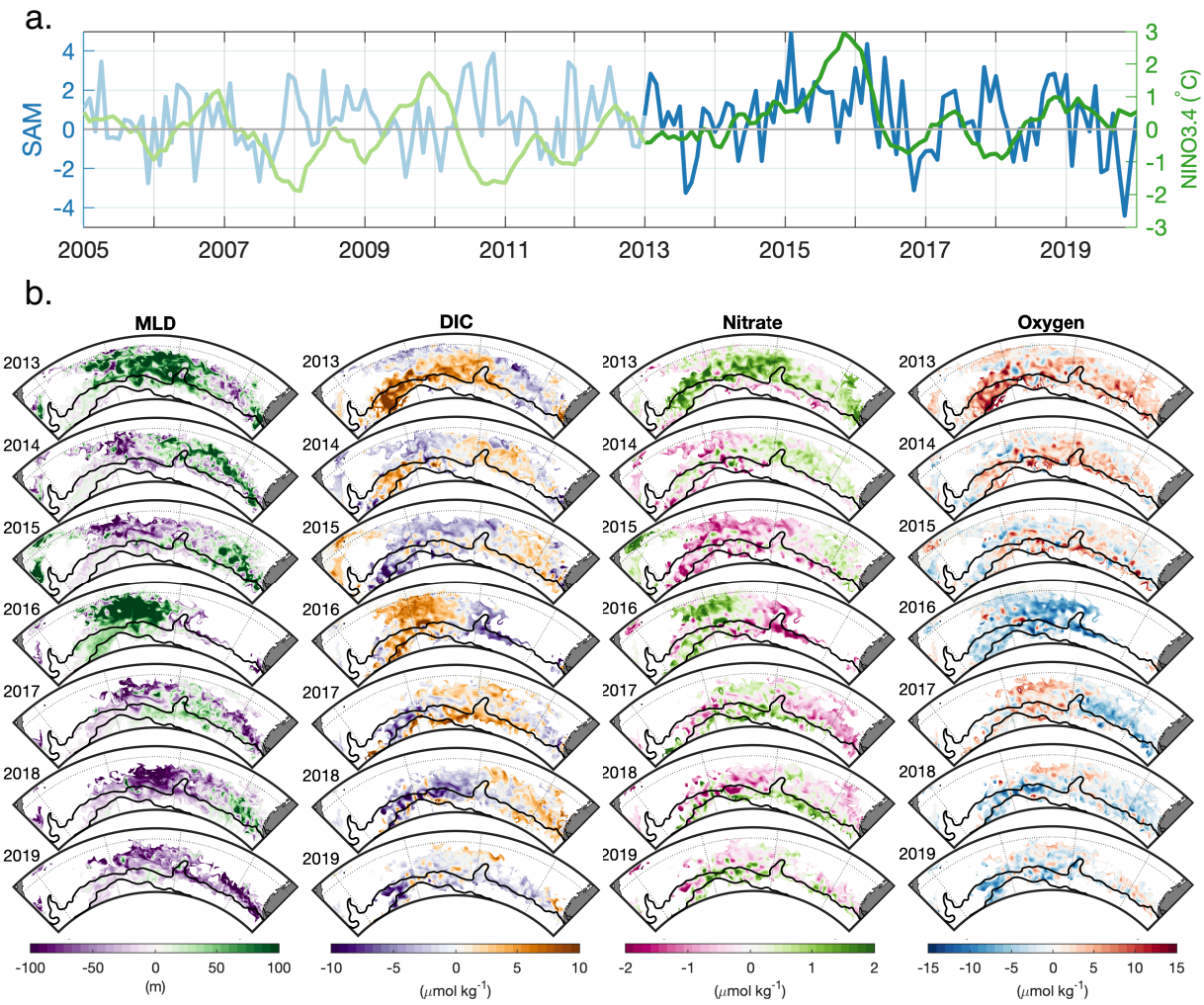


**Figure 6. Time series of ENSO, SAM, and BSOSE winter anomalies in MLD, DIC, nitrate, and oxygen.** (a) SAM (blue) and ENSO (green) indices are highlighted during the years covered by BSOSE. (b) Winter (AS) anomalies for MLD, DIC, nitrate, and oxygen demonstrate the combined influence of ENSO and SAM. Years and regions with deep MLD anomalies (green) are associated with higher DIC (orange) and nitrate (green). Spatial patterns of anomalies demonstrate a dipole between the central Pacific and southeast Pacific in many years, similar to a previously demonstrated pattern in SST, and Salinity (Cerovečki and Meijers, 2021).

anomalously shallow MLs in the central Pacific were associated with low DIC and low $NO_3^-$, while anomalously deep MLs in the eastern Pacific entrained high DIC and $NO_3^-$ waters. These anomaly maps suggest a link between SAM, ENSO, and biogeochemical anomalies, but the BSOSE time series is too short for more definitive attribution in the current study. Due to the relatively short time period covered by the BSOSE iteration 135 used for this analysis we chose to investigate interannual winter property anomalies rather than e.g. carrying out an EOF analysis, though an initial EOF analysis produced qualitatively similar results.

A time-series of the wintertime (Aug-Sep) mean ML property anomalies within the Pacific SAMW density range ($26.8 \leq \sigma_\theta < 27.05$ kg $m^{-3}$) considered separately in the central (45-64°S, 170-246°E) and southeast (45-64°S, 246-290°E) Pacific reveals a similar dipole pattern of DIC, nitrate, and oxygen as found in prior work considering physical properties (Figure 7). These two regions of the Pacific are not entirely out of phase, as the biogeochemical properties during the formation time period are not only governed by the local surface forcing that drives MLD anomalies, but also the properties from water formed in prior years incorporated through entrainment and lateral induction. The mean property anomalies of the Pacific are more closely correlated with Central Pacific than the southeast Pacific due to the larger volume of water formed in the central Pacific, in agreement with observational work by Cerovečki and Meijers (2021).

Oxygen time variability is more complicated as the fast gas exchange rate moves to restore air-sea equilibrium and replenish waters that are initially deficient in oxygen but have low temperatures and high solubility. In some years, such as 2016 when the strong El Niño and strongly positive SAM combined to produce anomalously deep MLs, the oxygen anomaly is negative, indicating that the entrainment signal was strong and persisted through the SAMW formation period. In other years, such as 2013, deep MLs are associated with positive oxygen anomalies. This dichotomy reflects the competing processes that impact oxygen in the upper ocean. In years with strong heat loss to the atmosphere, cooler temperatures will increase the solubility, which, coupled with strong winds driving high air-sea gas exchange rates, will tend to increase the oxygen concentration in the surface ocean. On the other hand, deeper mixing will entrain more low-oxygen water from below and the increased volume of the mixed layer will slow the change in oxygen concentration for a given air-sea flux. Years with reduced air-sea heat loss in the winter and shallower MLs are characterized by warmer temperatures and lower solubility but less entrainment of low-oxygen waters. A plot of SAMW oxygen concentration against potential temperature for

the Pacific and Pacific sub-regions reveals that the main signal is a fairly consistent offset relative to oxygen saturation of which approximately 1/3 is due to low SLP (Figure S3), implying that not only do oxygen concentrations closely follow interannual temperature changes, but also that the balance of the above processes leads to a consistent $\Delta[O_2]$ despite large changes in MLD and temperature. Both the magnitude of the $\Delta[O_2]$ offset and the lack of variability in BSOSE are consistent with float and ship-board observations (Figure 4).

Interestingly, the differences in biogeochemical property anomalies observed between the central and southeastern Pacific are more pronounced during the first half of the BSOSE time series than after 2016 (Figure 6). Physical and biogeochemical properties across the Pacific

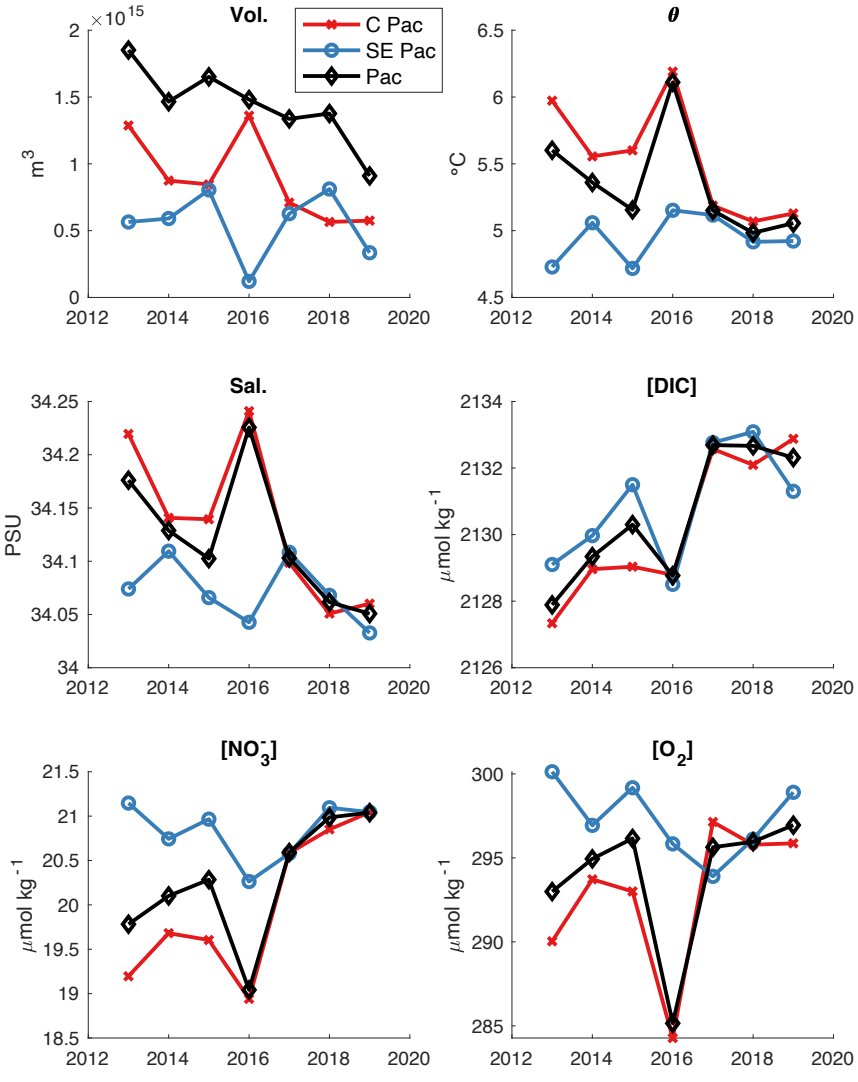


**Figure 7. SAMW Pacific formation properties in BSOSE**. Anomalies are mean winter (August and September) ML properties un the Pacific SAMW density range ($26.8 \leq \sigma_\theta < 27.05$ kg $m^{-3}$). Anomalies are calculated for the central (red line, 45-64°S, 170-246°E), southeast (blue, 45-64°S, 246-290°E), and overall Pacific (black, 45-64°S, 170-290°E) regions.

become uniform during the 2016 El Niño and remain so through 2017, 2018, and 2019. Homogenization during strong El Niño events in the south Pacific has been described previously using Argo observations (Cerovečki and Meijers 2021). This propagation of signals across the entire Pacific formation region is suggested by the apparent movement of anomalies from west to east in Figure 6. Advection of biogeochemical anomalies in BSOSE is more prominent when viewed in a Hovmöller diagram of the volume-weighted average upper ocean anomalies in the region where August-September MLs exceed 150m (Figure S4). Similar advective signals have been described in Argo observations of physical properties (Cerovečki and Meijers 2021) and previously in modeled temperature, salinity, and air-sea fluxes of oxygen and carbon dioxide (Verdy et al. 2007).

We are left with a framework where interannual variability in the biogeochemical properties of newly formed SAMW is influenced by a mix of local atmospheric forcing combined with the lateral induction of prior signals into the wintertime mixed layer. This mix of processes agrees with prior work on SAMW physical properties (Meijers et al. 2019; Cerovečki et al. 2019; Li et al. 2021) and a study demonstrating that surface fluxes are often not strong enough to change the physical properties of SAMW, due to the memory in the large volume of sub-surface water (Rintoul and England 2002). Advective propagation of anomalies can sometimes be interrupted by sufficiently large forcing events, but many biogeochemical anomalies do transit the entire Pacific SAMW formation region (Figure S4).

## 4. Conclusions

Here we use biogeochemical Argo float observations spanning a seven-year period to characterize for the first time the regional distribution of SAMW formation properties in the Pacific and Indian sectors, finding that the colder, fresher SAMW that forms in the Pacific is also higher in oxygen, nitrate, DIC, and $pCO_2$ than SAMW that forms in the Indian Ocean. The differences in formation properties between the Pacific and Indian Oceans reflect the differences in the density of SAMW formed in each region. The distribution of wintertime properties against density is consistent in both sectors, indicating that these property distributions predominantly represent a continuum of source water mass mixing between thermocline water, upwelled circumpolar deep water, and re-entrained SAMW.

In both the Pacific and Indian sectors, SAMW is undersaturated in oxygen at the time of formation, with slightly stronger undersaturation present in the Pacific formation regions. This undersaturation must be taken into account when calculating derived quantities that normally assume oxygen saturation at the time of water mass formation. This observed undersaturation appears fairly constant over the observed time period time and matches results from biogeochemical ocean state estimate BSOSE that suggest some consistent balance between undersaturation due to cooling or entrainment and replenishment by air-sea gas exchange that is maintained despite large interannual differences in oxygen concentration and SST.

There are large differences between the mean $\Delta pCO_2$ of newly formed SAMW estimated from profiling floats and that measured by underway shipboard observations. Float estimates of winter $\Delta pCO_2$ are on average ~17 μatm higher in this study than the limited SOCAT observations from the same formation regions. However, float observations are geographically more uniformly distributed over the SAMW formation regions, resulting in a wider range of properties than has been observed from shipboard observations. The bulk of these differences can be understood from the different sample distribution in the two datasets and there are no indications of systemic biases in the float data that are large enough to account for the differences between float and shipboard datasets. During the wintertime formation period, SAMW has a positive $\Delta pCO_2$ (average of SOCAT and float datasets) in the Pacific and a near neutral $\Delta pCO_2$ in the Indian formation region. This indicates that SAMW formation is not directly driving air-sea uptake of contemporary $CO_2$. The biogeochemical observations here provide for the first time the comparison data necessary to determine if models used to understand how anthropogenic carbon enters the ocean interior through mode and intermediate waters are accurately representing ocean biogeochemistry during mode water formation.

There are sufficient float biogeochemical observations to constrain mean wintertime formation properties but are not currently enough to investigate sub-regional or interannual variability. We thus used BSOSE output to explore spatial and temporal SAMW variability, focusing on the Pacific formation region. In the Pacific the link between climate modes of variability and SAMW response is the strongest and BSOSE representation of the magnitude and location of deep winter mixing in the Pacific was more similar to these from the RG-Argo than in the Indian sectors. Comparison between this study and Cerovečki and Meijers (2021) indicates that BSOSE reproduces the large-scale response of the MLD well, both in response to SAM and

ENSO and in the dipole pattern of variability between the central and southeast Pacific. BSOSE also accurately represents the relationships between biogeochemical properties and water mass density that we find in observations, giving good confidence that it can used to develop our understanding of the link between climate forcing and biogeochemical property variability in SAMW formation waters.

Interannual variability in the central and southeast Pacific biogeochemical formation properties display a see-saw pattern similar to that previously found in observations of physical properties. The suggested dipole pattern of biogeochemical properties relates well to the corresponding pattern in mixed layer depth and entrainment of deeper waters, with high nitrate and high DIC in regions and years with deep mixed layer anomalies and low nitrate and low DIC when the mixed layer is anomalously shallow. We expect that with more biogeochemical observations made in the Southern Ocean, these patterns will become evident in the observations as well. Interannual variability in oxygen concentration closely follows changes in ML temperature with a consistent undersaturation indicating that ML waters do not have time to equilibrate with the atmosphere regardless of whether there are anomalously deep or shallow MLDs.

Future work should focus on decomposing interannual variability in biogeochemical signals between local forcing processes and the influence of multi-year advective signals. A detailed understanding of the variability present in SAMW formation regions will help to understand how sensitive the interior volume is to changes in volume and properties of the individual formation regions and how strongly those variations are either modulated by the total interior SAMW volume or transported to the rest of the ocean.

SAMW is a critical water mass for the uptake of anthropogenic carbon and transport of oxygen and nutrients into the ocean interior. Improving our understanding of SAMW biogeochemical properties and their variability is of fundamental importance for improving our interpretation of interior ocean measurements, providing better validation for models, and therefore enabling new understanding of how SAMW functions in these global biogeochemical cycles.

**Acknowledgements:**

Float data were collected and made freely available by the Southern Ocean Carbon and Climate Observations and Modeling (SOCCOM) Project funded by the National Science Foundation, Division of Polar Programs (NSF PLR -1425989 and OPP-1936222), supplemented by NASA, and by the International Argo Program and the NOAA programs that contribute to it. The Argo Program is part of the Global Ocean Observing System. The Argo Program is part of the Global Ocean Observing System. The Surface Ocean CO2 Atlas (SOCAT,) is an international effort, endorsed by the International Ocean Carbon Coordination Project (IOCCP), the Surface Ocean Lower Atmosphere Study (SOLAS) and the Integrated Marine Biosphere Research (IMBeR) program, to deliver a uniformly quality-controlled surface ocean CO2 database. The many researchers and funding agencies responsible for the collection of data and quality control are thanked for their contributions to SOCAT. The specific SOCAT data used in this study were contributed by PIs K. Currie, A. Sutton, T. Trull, C. Sabine, T. Takahashi, C. Sweeney, S. C. Sutherland, T. Newberger, D. R. Munro, B. Tilbrook, J. Akl, and C. Neill. SOCAT data from the R/V Tangaroa were collected by the National Institute of Water and Atmospheric Research (funded by the New Zealand Ministry of Business, Innovation and Employment). SOCAT data from the R/V Gould and R/V Palmer were funded by the National Oceanic and Atmospheric Administration through the Global Ocean Monitoring and Observing Program and the Office of Oceanic and Atmospheric Research and by the National Science Foundation (grant numbers PLR 1341647 and 1543457). SOCAT underway data from Tilbrook, Akl and Neill were sourced through Australia's Integrated Marine Observing System (IMOS) – IMOS is enabled by the National Collaborative Research Infrastructure Strategy (NCRIS). Specific GLODAP data were collected on the R/Vs Knorr, Aurora Australis, Malcolm Baldrige, and M.-Dufresne. SMB was supported by NASA grants NNX17AI73G and 80NSSC22K0156 and benefited from support by the NOAA Climate Program Office's Climate Observations and Monitoring, Climate Variability and Predictability, and Global Ocean Monitoring and Observation programs (NA21OAR4310260). IC was supported by NASA grants 80NSSC22K0156 and 80NSSC19K1115.

**Conflict of Interest Statement**

The authors have no conflicts of interest to declare.

673

674 **Open Research**

675 Datasets used in this paper are from these references and the associated repositories:

676

677 Biogeochemical float data are from the May 2021 SOCCOM snapshot (Johnson et al, 2017;
678 doi.org/10.6075/J0T43SZG), along with the Drucker and Riser (2016) UW Argo Oxygen dataset
679 which is now included in the Argo dataset (https://argo.ucsd.edu/data/data-from-gdacs/). Gridded
680 Argo product by Roemmich and Gilson (2009) is available from https://argo.ucsd.edu/data/argo-
681 data-products/. Argo data were collected and made freely available by the International Argo
682 Program and the national programs that contribute to it (http://doi.org/10.17882/42182,
683 http://www.argo.ucsd.edu, http://argo.jcommops.org).

684

685 Shipboard data are from SOCAT v2021 (Bakker et al., 2016;
686 https://www.socat.info/index.php/data-access/) and GLODAP v2.2020 (Key et al., 2015; Olsen et
687 al., 2016; https://www.glodap.info/index.php/merged-and-adjusted-data-product/)

688

689 **References**

690

691 Álvarez, M., C. Lo Monaco, T. Tanhua, and others. 2009. Estimating the storage of
692 anthropogenic carbon in the subtropical Indian ocean: A comparison of five different
693 approaches. Biogeosciences **6**: 681–703. doi:10.5194/bg-6-681-2009
694 Bakker, D. C. E., B. Pfeil, C. S. Landa, and others. 2016. A multi-decade record of high-quality
695 fCO2 data in version 3 of the Surface Ocean CO2 Atlas (SOCAT). Earth Syst. Sci. Data **8**:
696 383–413. doi:10.5194/essd-8-383-2016
697 de Boyer Montégut, C., G. Madec, A. S. Fischer, A. Lazar, and D. Iudicone. 2004. Mixed layer
698 depth over the global ocean: An examination of profile data and a profile-based
699 climatology. J. Geophys. Res. **109**: C12003. doi:10.1029/2004JC002378
700 Broecker, W. S., and T. H. Peng. 1982. Tracers in the Sea., Lamont-Doherty Earth Observatory.
701 Bushinsky, S. M., A. R. Gray, K. S. Johnson, and J. L. Sarmiento. 2017. Oxygen in the Southern
702 Ocean From Argo Floats: Determination of Processes Driving Air-Sea Fluxes. J. Geophys.
703 Res. Ocean. **122**: 8661–8682. doi:10.1002/2017JC012923
704 Bushinsky, S. M., P. Landschützer, C. Rödenbeck, and others. 2019. Reassessing Southern
705 Ocean Air-Sea CO 2 Flux Estimates With the Addition of Biogeochemical Float
706 Observations. Global Biogeochem. Cycles **33**: 1370–1388. doi:10.1029/2019GB006176
707 Carter, B. R., R. A. Feely, S. K. Lauvset, and others. 2021. Preformed Properties for Marine
708 Organic Matter and Carbonate Mineral Cycling Quantification. Global Biogeochem. Cycles
709 **35**: 64–75. doi:10.1029/2020GB006623
710 Carter, B. R., R. A. Feely, N. L. Williams, and others. 2018. Updated methods for global locally
711 interpolated estimation of alkalinity, pH, and nitrate. Limnol. Oceanogr. Methods **16**: 119–

131. doi:10.1002/lom3.10232
Carter, B. R., L. D. Talley, and A. G. Dickson. 2014. Mixing and remineralization in waters detrained from the surface into Subantarctic Mode Water and Antarctic Intermediate Water in the southeastern Pacific. J. Geophys. Res. Ocean. **119**: 4001–4028. doi:10.1002/2013JC009355
Cerovečki, I., and M. R. Mazloff. 2016. The spatiotemporal structure of diabatic processes governing the evolution of Subantarctic Mode Water in the southern ocean. J. Phys. Oceanogr. **46**: 683–710. doi:10.1175/JPO-D-14-0243.1
Cerovečki, I., and A. J. S. Meijers. 2021. Strong quasi-stationary wintertime atmospheric surface pressure anomalies drive a dipole pattern in the Subantarctic ModeWater formation. J. Clim. 1–44. doi:10.1175/JCLI-D-20-0593.1
Cerovečki, I., A. J. S. Meijers, M. R. Mazloff, and others. 2019. The Effects of Enhanced Sea Ice Export from the Ross Sea on Recent Cooling and Freshening of the Southeast Pacific. J. Clim. **32**: 2013–2035. doi:10.1175/JCLI-D-18-0205.1
Dee, D. P., S. M. Uppala, A. J. Simmons, and others. 2011. The ERA-Interim reanalysis: Configuration and performance of the data assimilation system. Q. J. R. Meteorol. Soc. **137**: 553–597. doi:10.1002/qj.828
DeVries, T. 2014. The oceanic anthropogenic CO 2 sink: Storage, air-sea fluxes, and transports over the industrial era. Global Biogeochem. Cycles **28**: 631–647. doi:10.1002/2013GB004739
Dlugokencky, E. J., K. W. Thoning, P. M. Lang, and P. P. Tans. 2019. NOAA Greenhouse Gas Reference from Atmospheric Carbon Dioxide Dry Air Mole Fractions from the NOAA ESRL Carbon Cycle Cooperative Global Air Sampling Network.
Downes, S. M., C. Langlais, J. P. Brook, and P. Spence. 2017. Regional impacts of the westerly winds on Southern Ocean mode and intermediate water subduction. J. Phys. Oceanogr. **47**: 2521–2530. doi:10.1175/JPO-D-17-0106.1
Drucker, R., and S. C. Riser. 2016. In situ phase-domain calibration of oxygen Optodes on profiling floats. Methods Oceanogr. **17**: 1–34. doi:10.1016/j.mio.2016.09.007
Duteil, O., W. Koeve, A. Oschlies, and others. 2013. A novel estimate of ocean oxygen utilisation points to a reduced rate of respiration in the ocean interior. Biogeosciences **10**: 7723–7738. doi:10.5194/bg-10-7723-2013
Fay, A. R., N. S. Lovenduski, G. A. Mckinley, and others. 2018. Utilizing the Drake Passage Time-series to understand variability and change in subpolar Southern Ocean pCO 2. Biogeosciences Discuss. doi:https://doi.org/10.5194/bg-2017-489
Fay, A. R., G. A. McKinley, and N. S. Lovenduski. 2014. Southern Ocean carbon trends: Sensitivity to methods. Geophys. Res. Lett. **41**: 6833–6840. doi:10.1002/2014GL061324
Friedlingstein, P., M. W. Jones, M. O'Sullivan, and others. 2019. Global Carbon Budget 2019. Earth Syst. Sci. Data **11**: 1783–1838. doi:10.5194/essd-11-1783-2019
Gao, L., S. R. Rintoul, and W. Yu. 2018. Recent wind-driven change in Subantarctic Mode Water and its impact on ocean heat storage. Nat. Clim. Chang. **8**: 58–63. doi:10.1038/s41558-017-0022-8
García, H. E., and L. I. Gordon. 1992. Oxygen solubility in seawater: Better fitting equations. Limnol. Oceanogr. **37**: 1307–1312. doi:10.4319/lo.1992.37.6.1307
Garcia, H. E., R. A. Locarnini, T. P. Boyer, and others. 2010. World Ocean Atlas 2009 Volume 3: Dissolved Oxygen, Apparent Oxygen Utilization, and Oxygen Saturation.
Gray, A. R., K. S. Johnson, S. M. Bushinsky, and others. 2018. Autonomous Biogeochemical

758 Floats Detect Significant Carbon Dioxide Outgassing in the High-Latitude Southern Ocean.
759 Geophys. Res. Lett. **45**: 9049–9057. doi:10.1029/2018GL078013
760 Groeskamp, S., A. Lenton, R. Matear, B. M. Sloyan, and C. Langlais. 2016. Anthropogenic
761 carbon in the ocean—Surface to interior connections. Global Biogeochem. Cycles **30**:
762 1682–1698. doi:10.1002/2016GB005476
763 Gruber, N., D. Clement, B. R. Carter, and others. 2019a. The oceanic sink for anthropogenic CO
764 2 from 1994 to 2007. Science (80-. ). **363**: 1193–1199. doi:10.1126/science.aau5153
765 Gruber, N., S. C. Doney, S. R. Emerson, and others. 2009a. Adding oxygen to Argo: Developing
766 a global in-situ observatory for ocean deoxygenation and biogeochemistry. Ocean Obs '09.
767 Gruber, N., M. Gloor, S. E. Mikaloff Fletcher, and others. 2009b. Oceanic sources, sinks, and
768 transport of atmospheric CO 2. Global Biogeochem. Cycles **23**: n/a-n/a.
769 doi:10.1029/2008GB003349
770 Gruber, N., P. Landschützer, and N. S. Lovenduski. 2019b. The Variable Southern Ocean
771 Carbon Sink. Ann. Rev. Mar. Sci. **11**: 159–186. doi:10.1146/annurev-marine-121916-
772 063407
773 Hanawa, K., and L. Talley. 2001. Mode waters, p. 373–386. *In* International Geophysics.
774 Hartin, C. A., R. A. Fine, B. M. Sloyan, and others. 2011. Formation rates of Subantarctic mode
775 water and Antarctic intermediate water within the South Pacific. Deep. Res. Part I
776 Oceanogr. Res. Pap. **58**: 524–534. doi:10.1016/j.dsr.2011.02.010
777 Herraiz-Borreguero, L., and S. R. Rintoul. 2011. Subantarctic mode water: Distribution and
778 circulation. Ocean Dyn. **61**: 103–126. doi:10.1007/s10236-010-0352-9
779 van Heuven, S. M. A. C., D. Pierrot, J. W. B. Rae, E. Lewis, and D. W. R. Wallace. 2011.
780 Matlab program developed for CO2 system calculations. 530.
781 Ito, T., M. J. Follows, and E. A. Boyle. 2004. Is AOU a good measure of respiration in the
782 oceans? Geophys. Res. Lett. **31**: n/a-n/a. doi:10.1029/2004GL020900
783 Iudicone, D., K. B. Rodgers, Y. Plancherel, and others. 2016. The formation of the ocean's
784 anthropogenic carbon reservoir. Sci. Rep. **6**: 35473. doi:10.1038/srep35473
785 Iudicone, D., K. B. Rodgers, I. Stendardo, and others. 2011. Water masses as a unifying
786 framework for understanding the Southern Ocean Carbon Cycle. Biogeosciences **8**: 1031–
787 1052. doi:10.5194/bg-8-1031-2011
788 Johnson, K. S., J. N. Plant, L. J. Coletti, and others. 2017. Biogeochemical sensor performance in
789 the SOCCOM profiling float array. J. Geophys. Res. Ocean. **122**: 6416–6436.
790 doi:10.1002/2017JC012838
791 Kalnay, E., M. Kanamitsu, R. Kistler, and others. 1996. The NCEP/NCAR 40-Year Reanalysis
792 Project. Bull. Am. Meteorol. Soc. **77**: 437–471. doi:http://dx.doi.org/10.1175/1520-
793 0477(1996)077<0437:TNYRP>2.0.CO;2
794 Key, R. M., A. Olsen, S. van Heuven, and others. 2015. Global Ocean Data Analysis Project,
795 Version 2 (GLODAPv2). ORNL/CDIAC-162, NDP-093.
796 doi:10.3334/CDIAC/OTG.NDP093_GLODAPv2
797 Koch-Larrouy, A., R. Morrow, T. Penduff, and M. Juza. 2010. Origin and mechanism of
798 Subantarctic Mode Water formation and transformation in the Southern Indian Ocean.
799 Ocean Dyn. **60**: 563–583. doi:10.1007/s10236-010-0276-4
800 Koeve, W., and P. Kähler. 2016. Oxygen utilization rate (OUR) underestimates ocean
801 respiration: A model study. Global Biogeochem. Cycles **30**: 1166–1182.
802 doi:10.1002/2015GB005354
803 Landschützer, P., N. Gruber, D. C. E. Bakker, and others. 2013. A neural network-based estimate

of the seasonal to inter-annual variability of the Atlantic Ocean carbon sink. Biogeosciences **10**: 7793–7815. doi:10.5194/bg-10-7793-2013

Lauvset, S., K. Currie, N. Metzl, and others. 2017. SOCAT Quality Control Cookbook: for SOCAT version 7. SOCAT. doi:http://dx.doi.org/10.25607/OBP-1665

Lauvset, S. K., R. M. Key, A. Olsen, and others. 2016. A new global interior ocean mapped climatology: The 1° × 1° GLODAP version 2. Earth Syst. Sci. Data **8**: 325–340. doi:10.5194/essd-8-325-2016

Lenton, A., and R. J. Matear. 2007. Role of the Southern Annular Mode (SAM) in Southern Ocean CO2 uptake. Global Biogeochem. Cycles **21**: 1–17. doi:10.1029/2006GB002714

Li, Z., M. H. England, S. Groeskamp, I. Cerovečki, and Y. Luo. 2021. The Origin and Fate of Subantarctic Mode Water in the Southern Ocean. J. Phys. Oceanogr. 2951–2972. doi:10.1175/jpo-d-20-0174.1

Long, M. C., B. B. Stephens, K. McKain, and others. 2021. Strong Southern Ocean carbon uptake evident in airborne observations. Science (80-. ). **374**: 1275–1280. doi:10.1126/science.abi4355

Lovenduski, N. S., N. Gruber, S. C. Doney, and I. D. Lima. 2007. Enhanced CO 2 outgassing in the Southern Ocean from a positive phase of the Southern Annular Mode. Global Biogeochem. Cycles **21**: n/a-n/a. doi:10.1029/2006GB002900

Mackay, N., and A. Watson. 2021. Winter air-sea CO 2 fluxes constructed from summer observations of the Polar Southern Ocean suggest weak outgassing . J. Geophys. Res. Ocean. doi:10.1029/2020jc016600

McCartney, M. 1982. The subtropical recirculation of mode waters. J. Mar. Res **40**: 427–464.

McCartney, M. S. 1977. Subanarctic Mode Water, p. 103–119. *In* M. Angel [ed.], A Voyage of Discovery: George Deacon 70th Anniversary Volume.

Meijers, A. J. S., I. Cerovečki, B. A. King, and V. Tamsitt. 2019. A See-Saw in Pacific Subantarctic Mode Water Formation Driven by Atmospheric Modes. Geophys. Res. Lett. **46**: 13152–13160. doi:10.1029/2019GL085280

Mikaloff Fletcher, S. E., N. Gruber, A. R. Jacobson, and others. 2006. Inverse estimates of anthropogenic CO 2 uptake, transport, and storage by the ocean. Global Biogeochem. Cycles **20**: n/a-n/a. doi:10.1029/2005GB002530

Mikaloff Fletcher, S. E., N. Gruber, A. R. Jacobson, and others. 2007. Inverse estimates of the oceanic sources and sinks of natural CO2 and the implied oceanic carbon transport. Global Biogeochem. Cycles **21**: 1–19. doi:10.1029/2006GB002751

Mongwe, N. P., M. Vichi, and P. M. S. Monteiro. 2018. The seasonal cycle of p CO 2 and CO 2 fluxes in the Southern Ocean: diagnosing anomalies in CMIP5 Earth system models. Biogeosciences **15**: 2851–2872. doi:10.5194/bg-15-2851-2018

Morrison, A. K., T. L. Frölicher, and J. L. Sarmiento. 2015. Upwelling in the Southern Ocean. Phys. Today **68**: 27–32. doi:10.1063/PT.3.2654

Morrison, A. K., D. W. Waugh, A. M. Hogg, D. C. Jones, and R. P. Abernathey. 2022. Ventilation of the Southern Ocean Pycnocline. Ann. Rev. Mar. Sci. **14**: 405–430. doi:10.1146/annurev-marine-010419-011012

Olsen, A., R. M. Key, S. Van Heuven, and others. 2016. The global ocean data analysis project version 2 (GLODAPv2) - An internally consistent data product for the world ocean. Earth Syst. Sci. Data **8**: 297–323. doi:10.5194/essd-8-297-2016

Portela, E., N. Kolodziejczyk, C. Maes, and V. Thierry. 2020. Interior Water-Mass Variability in the Southern Hemisphere Oceans during the Last Decade. J. Phys. Oceanogr. **50**: 361–381.

doi:10.1175/JPO-D-19-0128.1
Primeau, F. W., M. Holzer, and T. DeVries. 2013. Southern Ocean nutrient trapping and the efficiency of the biological pump. J. Geophys. Res. Ocean. **118**: 2547–2564. doi:10.1002/jgrc.20181
Qu, T., S. Gao, and R. A. Fine. 2020. Variability of the Sub-Antarctic Mode Water Subduction Rate During the Argo Period. Geophys. Res. Lett. **47**. doi:10.1029/2020GL088248
Le Quéré, C., R. M. Andrew, P. Friedlingstein, and others. 2018. Global Carbon Budget 2018. Earth Syst. Sci. Data **10**: 2141–2194. doi:10.5194/essd-10-2141-2018
Raphael, M. N. 2004. A zonal wave 3 index for the Southern Hemisphere. Geophys. Res. Lett. **31**: 1–4. doi:10.1029/2004GL020365
Rintoul, S. R., and M. H. England. 2002. Ekman transport dominates local air-sea fluxes in driving variability of subantarctic mode water. J. Phys. Oceanogr. **32**: 1308–1321. doi:10.1175/1520-0485(2002)032<1308:ETDLAS>2.0.CO;2
Rödenbeck, C., R. F. Keeling, D. C. E. Bakker, and others. 2013. Global surface-ocean pCO2 and sea-Air CO2 flux variability from an observation-driven ocean mixed-layer scheme. Ocean Sci. **9**: 193–216. doi:10.5194/os-9-193-2013
Roemmich, D., and J. Gilson. 2009. The 2004-2008 mean and annual cycle of temperature, salinity, and steric height in the global ocean from the Argo Program. Prog. Oceanogr. **82**: 81–100. doi:10.1016/j.pocean.2009.03.004
Russell, J. L., and A. G. Dickson. 2003. Variability in oxygen and nutrients in South Pacific Antarctic Intermediate Water. Global Biogeochem. Cycles **17**: n/a-n/a. doi:10.1029/2000GB001317
Sabine, C. L., R. A. Feely, N. Gruber, and others. 2004. The Oceanic Sink for Anthropogenic CO 2. Science (80-. ). **305**: 367–371.
Sabine, C. L., and T. Tanhua. 2010. Estimation of Anthropogenic $CO_2$ Inventories in the Ocean. Ann. Rev. Mar. Sci. **2**: 175–198. doi:10.1146/annurev-marine-120308-080947
Sallée, J. B., K. G. Speer, and S. R. Rintoul. 2010. Zonally asymmetric response of the Southern Ocean mixed-layer depth to the Southern Annular Mode. Nat. Geosci. **3**: 273–279. doi:10.1038/ngeo812
Sarmiento, J. L., N. Gruber, M. A. Brzezinski, and J. P. Dunne. 2004. High-latitude controls of thermocline nutrients and low latitude biological productivity. Nature **427**: 56–60. doi:10.1038/nature10605
Sloyan, B. M., and S. R. Rintoul. 2001. The Southern Ocean Limb of the Global Deep Overturning Circulation*. J. Phys. Oceanogr. **31**: 143–173. doi:10.1175/1520-0485(2001)031<0143:TSOLOT>2.0.CO;2
Speer, K., S. R. Rintoul, and B. Sloyan. 2000. The Diabatic Deacon Cell*. J. Phys. Oceanogr. **30**: 3212–3222. doi:10.1175/1520-0485(2000)030<3212:TDDC>2.0.CO;2
Sutton, A. J., N. L. Williams, and B. Tilbrook. 2021. Constraining Southern Ocean CO2 Flux Uncertainty Using Uncrewed Surface Vehicle Observations. Geophys. Res. Lett. **48**: 1–9. doi:10.1029/2020GL091748
Tamsitt, V., I. Cerovečki, S. A. Josey, S. T. Gille, and E. Schulz. 2020. Mooring Observations of Air–Sea Heat Fluxes in Two Subantarctic Mode Water Formation Regions. J. Clim. **33**: 2757–2777. doi:10.1175/JCLI-D-19-0653.1
Verdy, A., S. Dutkiewicz, M. J. Follows, J. Marshall, and A. Czaja. 2007. Carbon dioxide and oxygen fluxes in the Southern Ocean: Mechanisms of interannual variability. Global Biogeochem. Cycles **21**: 1–10. doi:10.1029/2006GB002916

Verdy, A., and M. R. Mazloff. 2017. A data assimilating model for estimating Southern Ocean biogeochemistry. J. Geophical Res. Ocean. **122**: 1–22. doi:10.1002/2016JC012650

Williams, N. L., L. W. Juranek, R. A. Feely, and others. 2017. Calculating surface ocean pCO2 from biogeochemical Argo floats equipped with pH: An uncertainty analysis. Global Biogeochem. Cycles **31**: 591–604. doi:10.1002/2016GB005541

Williams, N. L., L. W. Juranek, R. A. Feely, and others. 2018. Assessment of the carbonate chemistry seasonal cycles in the Southern Ocean from persistent observational platforms. J. Geophys. Res. Ocean. **123**: 1–20. doi:10.1029/2017JC012917

Wolf, M. K., R. C. Hamme, D. Gilbert, I. Yashayaev, and V. Thierry. 2018. Oxygen Saturation Surrounding Deep Water Formation Events in the Labrador Sea From Argo-O 2 Data. Global Biogeochem. Cycles **32**: 635–653. doi:10.1002/2017GB005829

Wong, A. P. S., N. L. Bindoff, and J. A. Church. 1999. Large-scale freshening of intermediate waters in the Pacific and Indian oceans. Nature **400**: 440–443. doi:10.1038/22733

Zeebe, R. E., and D. A. Wolf-Gladrow. 2001. CO2 in Seawater: Equilibrium, Kinetics, Isotopes, Elsevier.